

AFRL-IF-RS-TR-1999-137

Final Technical Report

July 1999



LOW FREQUENCY MAGNETIC IMAGING DETECTOR FOR CONCEALED WEAPONS DETECTION

Systems & Processes Engineering Corporation

**Sponsored by
Advanced Research Projects Agency
DARPA Order No. D990**

APPROVED FOR PUBLIC RELEASE; DISTRIBUTION UNLIMITED.

The views and conclusions contained in this document are those of the authors and should not be interpreted as necessarily representing the official policies, either expressed or implied, of the Defense Advanced Research Projects Agency or the U.S. Government.

**AIR FORCE RESEARCH LABORATORY
INFORMATION DIRECTORATE
ROME RESEARCH SITE
ROME, NEW YORK**

DTIC QUALITY INSPECTED 4

19990907 118

This report has been reviewed by the Air Force Research Laboratory, Information Directorate, Public Affairs Office (IFOIPA) and is releasable to the National Technical Information Service (NTIS). At NTIS it will be releasable to the general public, including foreign nations.

AFRL-IF-RS-TR-1999-137 has been reviewed and is approved for publication.

APPROVED:



DAVID D. FERRIS, JR.
Project Engineer

FOR THE DIRECTOR:



JOHN V. MCNAMARA, Technical Advisor
Information & Intelligence Exploitation Division
Information Directorate

If your address has changed or if you wish to be removed from the Air Force Research Laboratory Rome Research Site mailing list, or if the addressee is no longer employed by your organization, please notify AFRL/IFEA, 32 Brooks Road, Rome, NY 13441-4114. This will assist us in maintaining a current mailing list.

Do not return copies of this report unless contractual obligations or notices on a specific document require that it be returned.

LOW FREQUENCY MAGNETIC IMAGING DETECTOR FOR CONCEALED
WEAPONS DETECTION

Byron Zollars
Michael Durrett
William Hallidy

Contractor: Systems & Processes Engineering Corporation
Contract Number: F30602-96-C-0005
Effective Date of Contract: 22 December 1995
Contract Expiration Date: 15 April 1997
Program Code Number: C141
Short Title of Work: Low Frequency Magnetic Imaging Detector for
Concealed Weapons Detection
Period of Work Covered: Dec 95 - Dec 96

Principal Investigator: Byron Zollars
Phone: (512) 306-1100X140
AFRL Project Engineer: David D. Ferris
Phone: (315) 330-4408

Approved for public release; distribution unlimited.

This research was supported by the Defense Advanced Research
Projects Agency of the Department of Defense and was monitored
by David D. Ferris, AFRL/IFEA, 32 Brooks Road, Rome, NY.

REPORT DOCUMENTATION PAGE			Form Approved OMB No. 0704-0188	
<small>Public reporting burden for this collection of information is estimated to average 1 hour per response, including the time for reviewing instructions, searching existing data sources, gathering and maintaining the data needed, and completing and reviewing the collection of information. Send comments regarding this burden estimate or any other aspect of this collection of information, including suggestions for reducing this burden, to Washington Headquarters Services, Directorate for Information Operations and Reports, 1215 Jefferson Davis Highway, Suite 1204, Arlington, VA 22202-4302, and to the Office of Management and Budget, Paperwork Reduction Project (0704-0188), Washington, DC 20503.</small>				
1. AGENCY USE ONLY (Leave blank)		2. REPORT DATE July 1999		3. REPORT TYPE AND DATES COVERED Final Dec 95 - Dec 96
4. TITLE AND SUBTITLE LOW FREQUENCY MAGNETIC IMAGING DETECTOR FOR CONCEALED WEAPONS DETECTION			5. FUNDING NUMBERS C - F30602-96-C-0005 PE - 62702E PR - C141 TA - 01 WU - P3	
6. AUTHOR(S) Byron Zollars, Michael Durrett, and William Hallidy				
7. PERFORMING ORGANIZATION NAME(S) AND ADDRESS(ES) Systems & Processes Engineering Corporation 401 Camp Craft Road Austin TX 78746			8. PERFORMING ORGANIZATION REPORT NUMBER N/A	
9. SPONSORING/MONITORING AGENCY NAME(S) AND ADDRESS(ES) Defense Advanced Research Projects Agency 3701 North Fairfax Drive Arlington VA 22203-1714			10. SPONSORING/MONITORING AGENCY REPORT NUMBER AFRL-IF-RS-TR-1999-137	
11. SUPPLEMENTARY NOTES Air Force Research Laboratory Project Engineer: David D. Ferris, Jr./IFEA/(315) 330-4408				
12a. DISTRIBUTION AVAILABILITY STATEMENT Approved for public release; distribution unlimited.			12b. DISTRIBUTION CODE	
13. ABSTRACT (Maximum 200 words) Military personnel, law-enforcement officers, and civilians face every-increasing dangers from persons carrying concealed handguns and other weapons. In direct correspondence with this danger is a need for more sophisticated means of detecting concealed weapons. We have developed a novel concealed-weapons detector based on the principle of low-frequency magnetic imaging. The detector is configured as a portal, and constructs an image of electrically conductive objectives transported through it with a potential spatial resolution of approximately 1 inch. Measurements on a breadboard version of the weapons detector have, to date, yielded a resolution of 2 inches. The detector is sensitive to all metals, semiconductors, and conductive composites. The measured conductivity image formed by the detector is combined with the video signal from a visible CCD camera to form a composite image of persons transiting the detector portal and the conductive objects they are carrying. Accompanying image recognition software could be used to determine the threat level of objects based upon shape, conductivity, and placement on the person of the carrier, and provide cueing, logging, or alarm functions to the operator if suspect weapons are identified. The low-power, low frequency emissions from the detector are at levels considered safe to humans and medical implants.				
14. SUBJECT TERMS Concealed Weapons Detection, Low Frequency Magnetic Imaging			15. NUMBER OF PAGES 48	
			16. PRICE CODE	
17. SECURITY CLASSIFICATION OF REPORT UNCLASSIFIED	18. SECURITY CLASSIFICATION OF THIS PAGE UNCLASSIFIED	19. SECURITY CLASSIFICATION OF ABSTRACT UNCLASSIFIED	20. LIMITATION OF ABSTRACT UL	

Table of Contents

1.0	Introduction	1
2.0	LFMI Concealed-Weapons Detector Concept.....	1
3.0	Low-Frequency Magnetic Imaging	2
3.1	LFMI Response in a Portal Geometry	2
4.0	Magnetic Field Modeling and Simulation	4
4.1	Numerical Technique.....	5
4.1.1	Quasi-Static Approximation.....	5
4.1.2	Lossy Dielectric Case.....	7
4.2	System Model.....	11
4.3	Sensor Response	16
4.4	Simulation Summary	17
5.0	Image Reconstruction.....	17
5.1	General Iterative Solution	18
5.2	Singular Value Decomposition	19
5.3	SVD Multi-Step Method.....	20
5.4	Hierarchical Image Reconstruction.....	21
5.5	Spatial Resolution Simulation.....	22
5.6	Discussion of Results.....	27
6.0	Experimental Results	28
6.1	Breadboard LFMI Apparatus	28
6.2	LFMI Magnetic Field Measurements.....	29
6.3	Material Response Measurements	30
6.4	Preliminary Imaging Measurements.....	30
6.5	Electronic Sensitivity	32
7.0	Phase 2 Program Plan	35

Executive Summary

Military personnel, law-enforcement officers, and civilians face ever-increasing dangers from persons carrying concealed handguns and other weapons. In direct correspondence with this danger is a need for more sophisticated means of detecting concealed weapons. We have developed a novel concealed-weapons detector based on the principle of low-frequency magnetic imaging. The detector is configured as a portal, and constructs an image of electrically conductive objects transported through it with a potential spatial resolution of approximately 1 inch. Measurements on a breadboard version of the weapons detector have, to date, yielded a resolution of 2 inches.

In operation, magnetic dipole radiation, emitted by transmitting antennas in the perimeter of the portal, is scattered from conductive objects and is picked up by receive antennas, also positioned around the portal. With sufficient measurements, each with a different geometry, a solution to the inverse scattering problem can be found. The result is an image of conductive objects in the detector. The detector is sensitive to all metals, semiconductors, and conductive composites. The measured conductivity image formed by the detector is combined with the video signal from a visible CCD camera to form a composite image of persons transiting the detector portal and the conductive objects they are carrying. Accompanying image recognition software could be used to determine the threat level of objects based upon shape, conductivity, and placement on the person of the carrier, and provide cueing, logging, or alarm functions to the operator if suspect weapons are identified. The low-power, low-frequency emissions from the detector are at levels considered safe to humans and medical implants.

The results of the breadboard tests demonstrate that we have the technology in hand to proceed to the brassboard phase with confidence. The inherent strengths of the LMFI concept are low cost (estimated at < \$10K) ease of setup and operation, imaging capability, resistance to countermeasures, and the ability to detect most practical threats, even when concealed within body cavities.

1.0 Introduction

With the proliferation of handguns and other concealable weapons, law enforcement agencies, government offices, and business owners are increasingly interested in applying more advanced means to prevent the transport of these weapons into their establishments. To answer this growing need, Systems & Processes Engineering Corporation (SPEC) is developing a concealed-weapons detector based on the proprietary technique of low-frequency magnetic imaging (LFMI). Analysis shows that a portal-based LFMI sensor has the potential to provide real-time imagery of conductive objects in the portal with a spatial resolution of one inch or smaller. Measurements made on a breadboard version of a doorway-sized LFMI sensor have validated the technique, and have yielded images of conductive objects with a spatial resolution of two inches. This report first presents an overview of the concealed-weapons detector currently under development, and discusses its features. Following that is a description of the LFMI physics and image reconstruction, with sample results from our numerical model. Finally, the results from recent measurements made with the breadboard concealed-weapons detector will be presented.

2.0 LFMI Concealed-Weapons Detector Concept

The LFMI concealed-weapons detector consists of magnetic-dipole antennas placed around the perimeter of a doorway or other portal. As shown in Figure 2-1, the antennas are placed in the portal with a nominal spacing of about 2 inches with each antenna connected to its own transceiver circuit. The transceivers are all connected via a common bus to a computer, which controls the configuration of antennas as transmitters and receivers. As transmitters, the antennas conduct an oscillating current, typically at a frequency of around 100 kHz (although this can be varied widely). System-wide clock distribution insures that the waveform of each transmitter has the same frequency and phase. As receivers, the antennas sense the induced emf from the oscillating magnetic field component normal to the plane of the antenna. The receivers are frequency and phase-locked to the transmitter signal, giving a high degree of rejection to out-of-band signals.

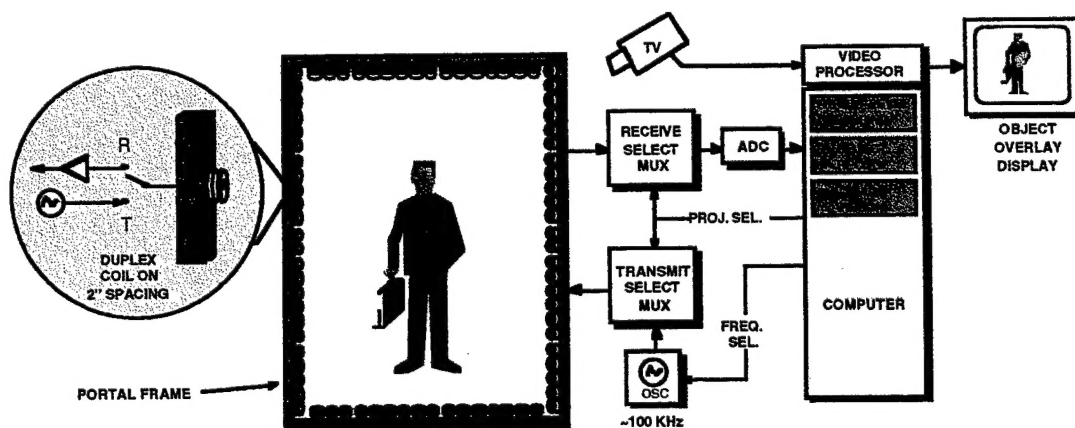


Figure 2-1 The LFMI Portal with associated subsystems

The computer orchestrates the data acquisition, configuring coils as transmitters, and measuring the response of the receivers at other positions in the portal. Multiple measurements, comprising many different transmitter-receiver angles, are performed. The data set is then reconstructed into an image of the conductivity in the plane of the portal. The measurement and image reconstruction proceed in real time, with an image update rate of approximately 10 Hz. As objects are transported through the portal, successive two-dimensional images are stacked to form a three-dimensional array; two dimensions of the array are inherently spatial, the third is implicitly spatial, and is scaled by the transport rate through the portal. A special set of antennas with orientation parallel to the plane are used to obtain object direction and a coarse estimate of speed. This information can be used to scale the third dimension of the array to reduce stretching or compression due to varying transport speeds.

As people walk through the portal, a visible CCD surveillance camera records their passage. The CCD camera video is overlaid with the corresponding projection from the three-dimensional LFMI data array. The result is an operator display that shows people transiting the portal with a superimposed image of the conductive objects that they are carrying. The three-dimensional array is simultaneously searched for threats with a pattern-matching algorithm that takes into consideration the object dimensions, orientation, and position. Imagery of the suspected weapon can be tagged with a different color, or will flash on the operator display. For unattended operation, alarms could alert mobile security personnel.

3.0 Low -Frequency Magnetic Imaging

3.1 LFMI Response in a Portal Geometry

Consider a portal in the x - y coordinate plane as depicted in Figure 3-1. The portal has a single magnetic dipole transmitter at location \mathbf{r}_T , and a single magnetic dipole receiver at location \mathbf{r}_R . In addition, assume the presence of a small perfectly conducting object of radius R located in the plane of the portal at location \mathbf{r}_O . The transmitter is assumed to be excited by a sinusoidally oscillating current such that it emits with a dipole moment amplitude of m_T [Amp m²]. The orientation of both the transmitter and receiver coils are along the x axis.

The dipole far-field approximation holds for distances more than a few coil diameters away from the transmitter, allowing the x and y components of the magnetic field amplitude at the object, due to the transmitter, to be calculated as

$$B_x(\bar{\mathbf{r}}_O; \bar{\mathbf{r}}_T) = \frac{\mu_0 m_T}{4\pi |\bar{\mathbf{r}}_O - \bar{\mathbf{r}}_T|^3} \{2 \cos^2 \beta - \sin^2 \beta\} \quad (3.1)$$

$$B_y(\bar{\mathbf{r}}_O; \bar{\mathbf{r}}_T) = \frac{3\mu_0 m_T}{4\pi |\bar{\mathbf{r}}_O - \bar{\mathbf{r}}_T|^3} \cos \beta \sin \beta \quad (3.2)$$

where β is the angle that $\mathbf{r}_O - \mathbf{r}_T$ makes with the x -axis, and μ_0 is the permeability of free space.

As the object experiences a changing magnetic field due to the transmitter, there will be an electric field induced in the object tangential to its surface. Since it is a perfect conductor, a surface current will flow that exactly opposes the component of the magnetic field normal to the object's surface at each point. If the object is small enough so that the transmitter field can be considered uniform, then the object (and its surface currents) are essentially an independent magnetic dipole emitter operating at the same frequency and in phase with the transmitter, with orientation angle in the plane of the portal

$$\phi = \tan^{-1} \left[\frac{B_y(\bar{r}_O; \bar{r}_T)}{B_x(\bar{r}_O; \bar{r}_T)} \right] \quad (3.3)$$

and effective dipole moment amplitude

$$m_O = \frac{2\pi R^3 \sqrt{B_x(\bar{r}_O; \bar{r}_T)^2 + B_y(\bar{r}_O; \bar{r}_T)^2}}{\mu_0} \quad (3.4)$$

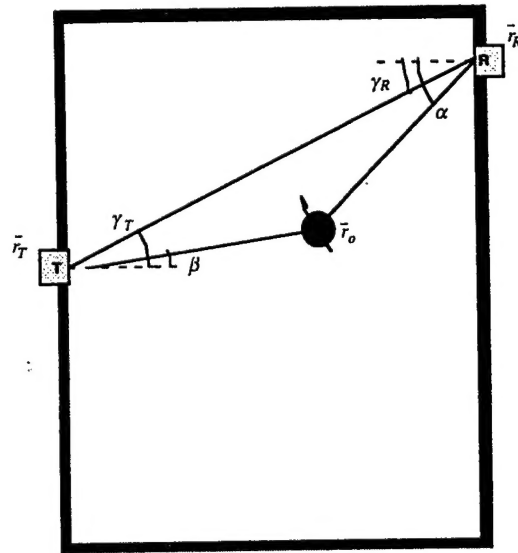


Figure 3-1 Geometry of object in the portal

The receiver now measures the x -component of the dipole field from both the transmitter and the object. If we assume that the receiver signal with no object in the portal is measured during a calibration step, it can subsequently be subtracted from the total receiver measurement to yield only the portion of the measurement due to the object. Call this quantity the signal S at \bar{r}_R , due to object at \bar{r}_O , with transmitter at \bar{r}_T . After some algebra, the signal can be expressed as

$$S(\bar{r}_R; \bar{r}_O; \bar{r}_T) = \frac{\mu_0 m_O}{4\pi |\bar{r}_R - \bar{r}_O|^3} \left\{ [2\cos^2(\phi - \alpha) - \sin^2(\phi - \alpha)] \cos \phi - 3\cos(\phi - \alpha) \sin(\phi - \alpha) \sin \phi \right\} \quad (3.5)$$

The key to the linear formulation of the imaging equations lies in the recognition that the right-hand side of Equation 3.5 is purely a function of geometry. Now, by superposition, the signal at \mathbf{r}_R , with transmitter at \mathbf{r}_T , due to an ensemble of N small objects at locations \mathbf{r}_{oi} is just the sum of geometric factors

$$S(\{\bar{\mathbf{r}}_R, \bar{\mathbf{r}}_T\}) = \sum_{i=1}^N S(\bar{\mathbf{r}}_R; \bar{\mathbf{r}}_{oi}; \bar{\mathbf{r}}_T) = \sum_{i=1}^N G(\bar{\mathbf{r}}_{oi}; \{\bar{\mathbf{r}}_R, \bar{\mathbf{r}}_T\}) \quad (3.6)$$

Here we have neglected the small magnetic interaction between adjacent object's dipole fields. Extending this argument one step further, we break the entire plane of the portal into a rectangular array of M pixels, with locations denoted (perhaps in raster order) as \mathbf{r}_{pj} , where $j=1,2,\dots,M$. If we now constrain the locations of the N objects to the nearest pixel locations, we can rewrite Equation 6 as

$$S(\{\bar{\mathbf{r}}_R, \bar{\mathbf{r}}_T\}) = \sum_{j=1}^M G(\bar{\mathbf{r}}_{pj}; \{\bar{\mathbf{r}}_R, \bar{\mathbf{r}}_T\}) P_j \quad (3.7)$$

where P_j is a vector of M elements, consisting of ones in the N locations corresponding to object positions, and zeros elsewhere. This equation holds for all possible pairings of transmitters and receivers, so it is easy to generalize further to a system of vector products, one equation for each receiver-transmitter pair. If there are Q such pairs, the system becomes

$$S(\{\bar{\mathbf{r}}_R, \bar{\mathbf{r}}_T\}_k) = \sum_{j=1}^M G(\bar{\mathbf{r}}_{pj}; \{\bar{\mathbf{r}}_R, \bar{\mathbf{r}}_T\}_k) P_j; \quad k = 1, 2, \dots, Q \quad (3.8)$$

For a static measurement geometry, i.e. a fixed set of transmitters and receivers, the G factors are all constants, and so Equation 3.8 can be written as a matrix equation relating the signal measurements with which pixels in the portal contain an object.

$$\mathbf{S}_{Q \times 1} = \mathbf{G}_{Q \times M} \mathbf{P}_{M \times 1} \quad (3.9)$$

Given a set of receiver measurements in the \mathbf{S} matrix, the system of linear equations in Equation 3.9 can be solved for the pixels that contain an object by finding the generalized inverse of the \mathbf{G} matrix. The pixel vector \mathbf{P} can then be rasterized to yield the image of the conductive objects in the portal. In general, the \mathbf{P} vector can assume values other than zero or one, indicating the strength of the radiating induced dipole in the portal.

$$\mathbf{P}_{M \times 1} = \hat{\mathbf{G}}_{M \times Q} \mathbf{S}_{Q \times 1} \quad (3.10)$$

4.0 Magnetic Field Modeling and Simulation

Magnetic field scattering calculations are required in order to provide numerical simulations for use in imaging analysis. These calculations also permit rapid demonstration of alternative portal geometries. The type, number, location, and orientation of transmitters

and receivers, the size and type of system geometry, and the type, location, and number of targets are all variable parameters in the model.

4.1 Numerical Technique

The Method of Moments was used to provide a numerical solution to the electromagnetic field equations. This method, which provides a numerical solution to integral equations for the fields using a free space Green's function, works well for compact, arbitrarily shaped targets.

4.1.1 Quasi-Static Approximation

The modulation frequencies used in the magnetic imaging detector are rather low, around 100 kHz. The corresponding wavelengths in air are therefore around 3 km, while the sizes of the imaging apparatus and of the targets to be imaged are of the order of 1 m to 2 cm. Under these conditions, the fields scattered by metallic materials and low dielectric constant magnetic materials such as ferrites can be determined within the quasi-static approximation. This approximation decouples the electromagnetic fields, so that we may solve equations involving only the magnetic fields of the source and target. For this case, the magnetic field of a volume distribution of current in an arbitrarily shaped region, as shown in Figure 4-1, may be determined by integration.

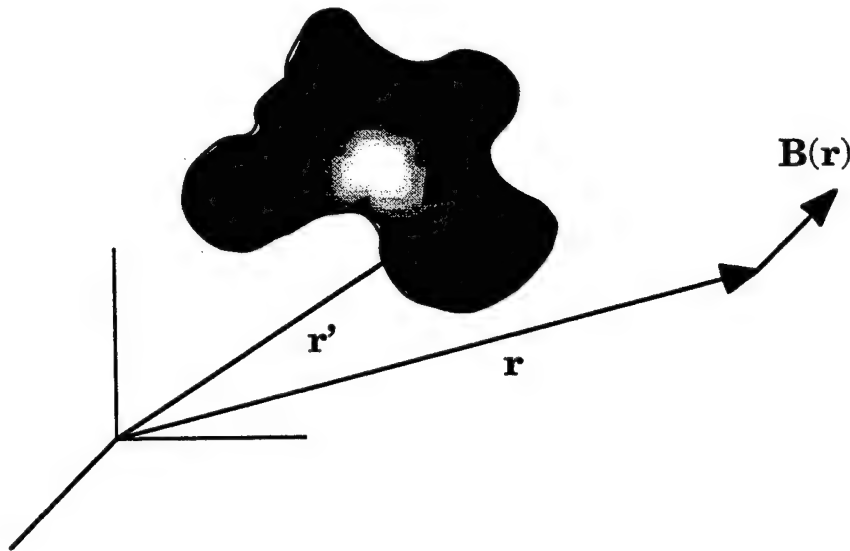


Figure 4-1: Illustration of the magnetic field produced by a volume distribution of currents in an arbitrarily shaped object

Outside of the object, the integral for the field may be written:

$$\mathbf{B}(\mathbf{r}) = \frac{\mu_0}{4\pi} \int_{\text{Volume}} \frac{\mathbf{j}(\mathbf{r}') \times (\mathbf{r} - \mathbf{r}')}{\|\mathbf{r} - \mathbf{r}'\|^3} dV, \quad (4.1)$$

where $\mathbf{B}(\mathbf{r})$ is the field at the point \mathbf{r} in Figure 4-1, $\mathbf{j}(\mathbf{r}')$ is the current density at \mathbf{r}' , $\mu_0/4\pi = 10^{-7}$ H/m and the integral is taken over the volume of the object.

For perfect conductors and for non-conductive, homogeneous, magnetic materials, the currents in the target reduce to currents on its surface. Away from the surface, the total field, including the source (transmitter) field, may be written:

$$\mathbf{B}(\mathbf{r}) = \mathbf{B}_{\text{Source}}(\mathbf{r}) + \frac{\mu_0}{4\pi} \int_{\text{Surface}} \frac{\mathbf{k}(\mathbf{r}') \times (\mathbf{r} - \mathbf{r}')}{\|\mathbf{r} - \mathbf{r}'\|^3} dS, \quad (4.2)$$

where \mathbf{k} is the surface current density. The scattered field is the second member of the right hand side of Equation 4.2. Thus, the scattered field may be determined by numerical integration once the surface currents on the target are known.

In the limit, as \mathbf{r} approaches the surface, we have

$$\mathbf{B}_{\pm}(\mathbf{r}) = \mathbf{B}_{\text{Source}}(\mathbf{r}) + \frac{\mu_0}{4\pi} \int_{\text{Surface}^*} \frac{\mathbf{k}(\mathbf{r}') \times (\mathbf{r} - \mathbf{r}')}{\|\mathbf{r} - \mathbf{r}'\|^3} dS \pm \frac{\mu_0}{2} \mathbf{k}(\mathbf{r}) \times \mathbf{n}(\mathbf{r}) \quad (4.3)$$

where \mathbf{n} is the outward unit normal to the surface, the plus/minus sign applies just outside/inside the surface and * indicates the principal value of the integral.

In order to evaluate the integral equation 4.3 for the surface currents, we approximate the target surface by dividing it into planar patches, small enough so that \mathbf{k} is essentially constant on each patch. (For non-simply connected magnetic targets, any inner surfaces must also be divided into patches.) Equation 3 therefore takes the form:

$$\begin{aligned} \mathbf{B}_{\pm}(\mathbf{r}_m) = & \mathbf{B}_{\text{Source}}(\mathbf{r}_m) + \frac{\mu_0}{4\pi} \int_{\Delta_m^*} \frac{\mathbf{k}(\mathbf{r}_m') \times (\mathbf{r}_m - \mathbf{r}_m')}{\|\mathbf{r}_m - \mathbf{r}_m'\|^3} dS' \\ & + \frac{\mu_0}{4\pi} \sum_{n \neq m} \int_{\Delta_n^*} \frac{\mathbf{k}_n \times (\mathbf{r}_m - \mathbf{r}_n)}{\|\mathbf{r}_m - \mathbf{r}_n\|^3} dS \pm \frac{\mu_0}{2} \mathbf{k}_m \times \mathbf{n}_m \end{aligned} \quad (4.4)$$

where Δ_m denotes the m th patch. We note here that for planar patches we have:

$$\mathbf{n}_m \times \int_{\Delta_m^*} \frac{\mathbf{k}(\mathbf{r}_m') \times (\mathbf{r}_m - \mathbf{r}_m')}{\|\mathbf{r}_m - \mathbf{r}_m'\|^3} dS' = 0. \quad (4.5)$$

In order to determine the surface currents it is necessary to impose boundary conditions appropriate to the target. For a perfect conductor, Equation 4.4 must satisfy:

$$\mathbf{B}_{-}(\mathbf{r}_m) = 0, \quad (4.6)$$

and

$$\mathbf{n}_m \times \mathbf{B}_{+}(\mathbf{r}_m) = \mu_0 \mathbf{k}_m \quad (4.7)$$

for all m .

Substituting Equation 4.7 into Equation 4.4, taking the cross product with the normal to the surface patch Δ_m , and employing Equations 4.5 and 4.6, we obtain the following set of equations for the surface currents:

$$\mu_0 \mathbf{k}_m = 2 \left[\mathbf{n}_n \times \mathbf{B}_{\text{Source}}(\mathbf{r}_m) + \frac{\mu_0}{4\pi} \sum_{n \neq m} \mathbf{n}_n \times (\mathbf{k}_n \times \mathbf{S}_{mn}) \right] \quad (4.8)$$

where

$$\mathbf{S}_{mn} = \int_{\Delta_n} \frac{(\mathbf{r}_m - \mathbf{r}_n)}{\|\mathbf{r}_m - \mathbf{r}_n\|^3} dS \approx \frac{(\mathbf{r}_m - \mathbf{r}_n)}{\|\mathbf{r}_m - \mathbf{r}_n\|^3} \delta S_n, \quad (4.9)$$

and δS_n is the area of the n th patch. For the magnetic non-conductor, the relevant boundary conditions are:

$$\frac{1}{\mu_0} \mathbf{n}_m \times \mathbf{B}_+(\mathbf{r}_m) = \frac{1}{\mu} \mathbf{n}_m \times \mathbf{B}_-(\mathbf{r}_m) \quad (4.10)$$

where μ is the permeability of the target. Employing Equation 4.4 in Equation (10) yields a set of equations for the surface currents:

$$\mu_0 \mathbf{k}_m = -2 \left(\frac{\mu - \mu_0}{\mu + \mu_0} \right) \left[\mathbf{n}_n \times \mathbf{B}_{\text{Source}}(\mathbf{r}_m) + \frac{\mu_0}{4\pi} \sum_{n \neq m} \mathbf{n}_n \times (\mathbf{k}_n \times \mathbf{S}_{mn}) \right] \quad (4.11)$$

The similarity between Equations 4.8 and 4.11 has been exploited to allow the same computer program to be used for the determination of the scattered fields for the metallic and the magnetic case.

4.1.2 Lossy Dielectric Case

The quasi-static approximation fails for materials which have a sufficiently large dielectric constant. This, of course, includes lossy dielectrics such as graphite composites. For such materials we must solve the full, time harmonic equations for the electromagnetic fields.

As the fields penetrate the target, we might expect that it would be necessary to solve for a volume distribution of currents. This is certainly one type of approach that can be used. However, it is possible to define the fields completely both within and outside the target by solving for currents on the boundary of the volume containing the target. The method is justified by the uniqueness theorem and the equivalence principle which are briefly described below.

The uniqueness theorem of electromagnetics tells us that the fields in a region are determined by sources within the region together with the tangential components of the electric and/or the magnetic field on the boundary of the region.

The equivalence principle is a sort of non-uniqueness theorem for the sources outside the region of interest. That is to say, there are many source distributions *outside* a region which will lead to the same tangential components of the fields on the boundary of the region. If we extend the field equations to admit (fictitious) magnetic currents, it becomes possible to choose these electric and magnetic sources to be distributed as surface currents on the boundary of the region. In order to uniquely specify these surface currents, we extend the region to include the outside by specifying the values of the fields outside the

original region. This is usually (but not necessarily) done by requiring the outside fields to be identically zero.

In Figure 4-2 we depict the original problem that we wish to solve. In our case, the permittivity and permeability outside of the target and the permeability within the target have their free space values. The permittivity within the target is a complex constant. The total fields outside of and within the target consist of an incident field, \mathbf{H}_{inc} , produced by the source, and the scattered field, \mathbf{H}_s , produced by the target. The incident source is confined to a compact region near the target. The unit vector, \mathbf{n} , denotes the direction of the normal to the boundary of the target. In order to solve this problem, we divide it into an exterior equivalence problem, **I**, shown in Figure 4-3 and an interior equivalence problem, **II**, shown in Figure 4-4.

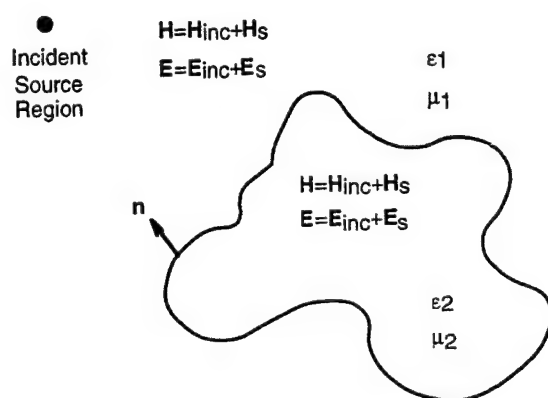


Figure 4-2: The original problem.

In Figure 4-3, we see that for problem **I** the fields within the target are required to be zero. The permittivity and permeability within the target region are taken to have the same values as they do outside for the original problem. This allows us to use the free space Green's function to express the fields in terms of the currents.

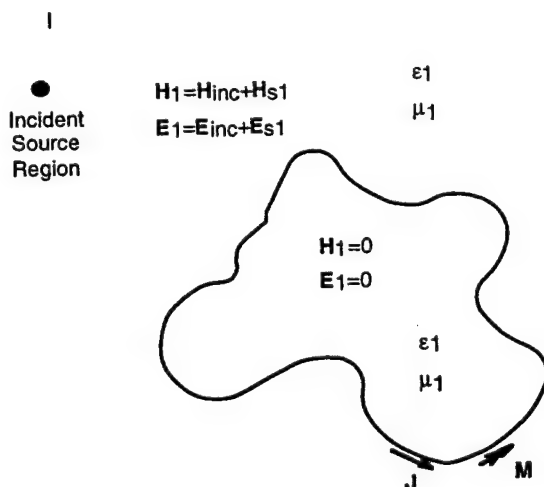


Figure 4-3: The exterior equivalence problem.

At each point of the boundary, the electric surface current, \mathbf{J} , and the magnetic surface current, \mathbf{M} , satisfy the equations:

$$\begin{aligned}\mathbf{J} &= \mathbf{n} \times [\mathbf{H}_{\text{inc}} + \mathbf{H}_{s1}^+(\mathbf{J}) + \mathbf{H}_{s1}(\mathbf{M})] \\ \mathbf{M} &= [\mathbf{E}_{\text{inc}} + \mathbf{E}_{s1}^+(\mathbf{M}) + \mathbf{E}_{s1}(\mathbf{J})] \times \mathbf{n}\end{aligned}\quad (4.12)$$

where the contributions to the fields from the electric and magnetic surface currents are shown as separate terms and where the + superscript denotes that the field is evaluated just outside the boundary. Unscripted fields are continuous across the boundary.

II

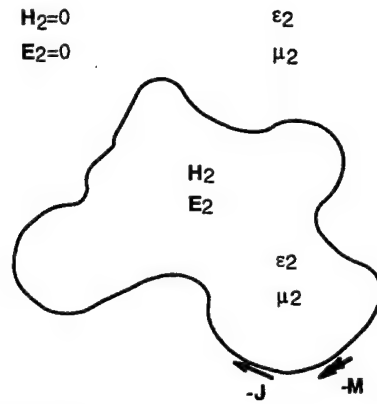


Figure 4-4: The interior equivalence problem

For problem II, Figure 4-4 shows that the fields outside the target are set to zero. The permittivity and permeability outside are given the values they had within the target for the original problem. This permits a simple modification of the free space Green's function to be used to determine the fields in terms of the currents. In order to satisfy the boundary conditions of the original problem, the tangential components of the fields just within the surface of problem II must equal those just outside the surface of problem I. This requires that the currents for problem II are the negatives of those for problem I. We therefore have:

$$\begin{aligned}\mathbf{J} &= \mathbf{n} \times [\mathbf{H}_2^-(-\mathbf{J}) + \mathbf{H}_2(-\mathbf{M})] \\ \mathbf{M} &= [\mathbf{E}_2^-(-\mathbf{M}) + \mathbf{E}_2(-\mathbf{J})] \times \mathbf{n}\end{aligned}\quad (4.13)$$

where a negative (positive) subscript denotes the field evaluated just inside (outside) the boundary.

Equating the tangential components of the fields in Equations 4.12 and 4.13 and recognizing that, as the fields are linear functions of the currents, they change sign with the currents, we find:

$$\begin{aligned}\hat{\mathbf{n}} \times \left[\mathbf{E}_{s1}(\mathbf{J}) + \mathbf{E}_2(\mathbf{J}) + \mathbf{E}_{s1}^-(\mathbf{M}) + \mathbf{E}_2^+(\mathbf{M}) \right] &= -\hat{\mathbf{n}} \times \mathbf{E}_{\text{inc}} \\ \hat{\mathbf{n}} \times \left[\mathbf{H}_{s1}^-(\mathbf{J}) + \mathbf{H}_2^+(\mathbf{J}) + \mathbf{H}_{s1}(\mathbf{M}) + \mathbf{H}_2(\mathbf{M}) \right] &= -\hat{\mathbf{n}} \times \mathbf{H}_{\text{inc}}\end{aligned}\quad (4.14)$$

Equations 4.14 are satisfied at each point of the boundary.

The fields produced by the electric surface currents may be written in terms of the currents by means of the vector and scalar potentials \mathbf{A} and V_e :

$$\begin{aligned}\mathbf{E}(\mathbf{J}, \mathbf{r}) &= i\omega\mathbf{A}(\mathbf{r}) - \nabla V_e(\mathbf{r}) \\ \mathbf{H}(\mathbf{J}, \mathbf{r}) &= \frac{1}{\mu} \nabla \times \mathbf{A}(\mathbf{r})\end{aligned}\quad (4.15)$$

$$\begin{aligned}\mathbf{A}(\mathbf{r}) &= \frac{\mu}{4\pi} \iint \mathbf{J}(\mathbf{r}') G(\mathbf{r}, \mathbf{r}') dS' \\ V_e(\mathbf{r}) &= \frac{1}{4\pi\epsilon} \iint \rho_e(\mathbf{r}') G(\mathbf{r}, \mathbf{r}') dS'\end{aligned}\quad (4.16)$$

where, in Equation 4.16, the charge, ρ_e , is related to the surface current, \mathbf{J} , by the continuity equation

$$\nabla \cdot \mathbf{J} = i\omega\rho_e \quad (4.17)$$

and where ω is the angular frequency of the time harmonic fields and currents. The function $G(\mathbf{r}, \mathbf{r}')$ is the Green's function for the problem:

$$G(\mathbf{r}, \mathbf{r}') = \frac{e^{ik|\mathbf{r} - \mathbf{r}'|}}{|\mathbf{r} - \mathbf{r}'|} \quad (4.18)$$

where k , the wavevector appropriate to the problem, is defined in terms of the permittivity and permeability as:

$$k = \omega\sqrt{\epsilon\mu} \quad (4.19)$$

Equations for the fields produced by the magnetic current are given below as Equations 4.20 and 4.21.

$$\begin{aligned}\mathbf{E}(\mathbf{M}, \mathbf{r}) &= -\frac{1}{\epsilon} \nabla \times \mathbf{F}(\mathbf{r}) \\ \mathbf{H}(\mathbf{M}, \mathbf{r}) &= i\omega\mathbf{F}(\mathbf{r}) - \nabla V_m(\mathbf{r})\end{aligned}\quad (4.20)$$

$$\begin{aligned}\mathbf{F}(\mathbf{r}) &= \frac{\epsilon}{4\pi} \iint \mathbf{M}(\mathbf{r}') G(\mathbf{r}, \mathbf{r}') dS' \\ V_m(\mathbf{r}) &= \frac{1}{4\pi\mu} \iint \rho_m(\mathbf{r}') G(\mathbf{r}, \mathbf{r}') dS'\end{aligned}\quad (4.21)$$

Equation 4.22 is the continuity equation for the magnetic charge.

$$\nabla \cdot \mathbf{M} = i\omega\rho_m \quad (4.22)$$

When Equations 4.15 through 4.22 are substituted into Equation 4.14 a set of integro-differential equations defining the surface currents are found. These equations can be solved numerically by breaking the surface into triangular patches. However, because of the presence of derivatives in the equations, the currents on each triangular patch should be chosen to be represented by linear functions with continuous components normal to the common sides of adjacent triangles. Once the currents have been found, the scattered magnetic fields in the exterior region may be determined by numerical integration of Equations 4.15, 4.16, 4.20, and 4.21. Numerical solutions of the field equations will be developed in the next phase of the research.

It should be noted that the procedure just described may be modified in a straightforward manner to permit determination of the fields produced by scattering from metallic objects embedded in lossy dielectrics.

4.2 System Model

The computer simulation allows arbitrary transmitter, receiver, and target geometries and locations. However, in order to model our magnetic imaging system, the system geometry was constructed as illustrated in Figure 4-5. The transmitters and receivers were modeled as magnetic dipoles; each receiver is sensitive to one component of the local magnetic field. The transceivers were distributed uniformly around a square of length 1 m on a side, with 20 elements per side. The transceivers were oriented with their dipoles in the plane of the square and locally perpendicular to the side where they were located. (The dipole orientations were varied in some of the imaging simulations.)

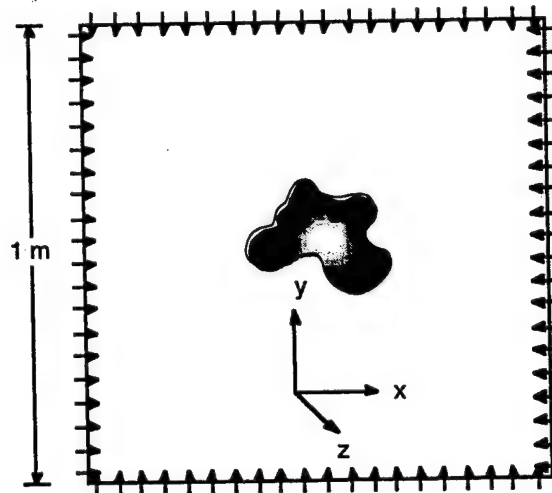


Figure 4-5: Simulated system geometry

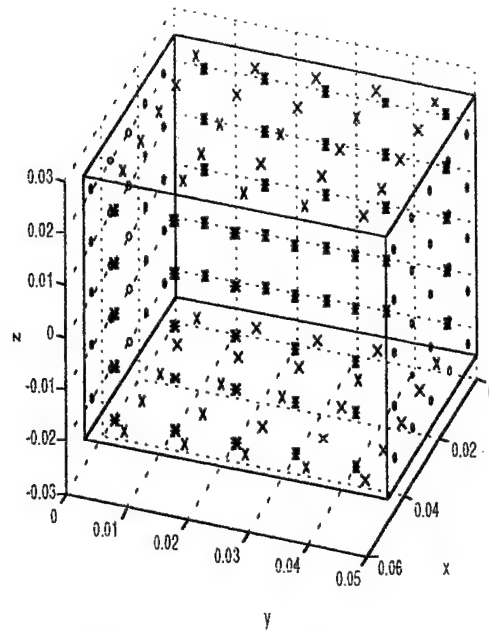


Figure 4-6: Simple target geometry

The target geometries could also be chosen arbitrarily. For our imaging system tests, the target was usually chosen to be a simple box that straddled the $z=0$ plane near the center of the square. Figure 4-6 depicts one such target, a cube 5 cm on a side. The coordinate system is shown rotated from that of Figure 4-5 so that the z axis points up instead of out and the axes are not drawn in the same scale. All dimensions are in meters. The red crosses, blue stars and green circles are sample points that were chosen for the particular simulation run. They each lie at the center of a local rectangular patch which was used for the numerical computation.

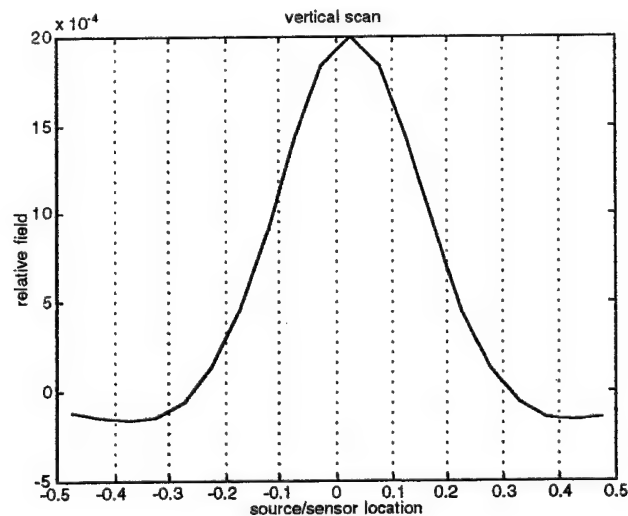


Figure 4-7: A vertical scan of the target shown in Figure 4-6

Examples of two scans through the target for the system geometry depicted in Figure 4-5 are shown in Figures 4-7 and 4-8. The vertical scan shown in Figure 4-7 was made by activating each transmitter located on the left hand side of the square in succession, starting at the top and proceeding to the bottom, and determining the relevant scattered field component at the receiver located horizontally across from the active transmitter. The horizontal axis in the figure gives the location in meters of the active transmitter and receiver on their respective sides. The vertical axis gives the value of the scattered field relative to the magnitude of the direct field. The peak value occurs when the target is directly between the transmitter and receiver. A zero value indicates that the scattered field has no component in the receiver direction. Negative values indicate that the orientation of the scattered field component is flipped 180 degrees with respect to the receiver direction.

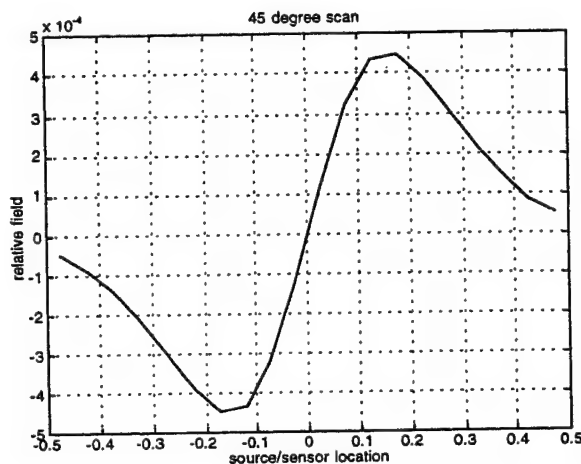


Figure 4-8: A 45 degree scan of the target shown in Figure 4-6

The 45 degree scan shown in Figure 4-8 was made by activating transmitters in the same manner as described for Figure 4-7, and successively activating receivers along the top edge starting at the left in Figure 4-5. Thus each active transmitter/receiver pair was located along a line sloped positively at 45 degrees to the sides of the square. The horizontal axis in the figure again gives the location in meters of the transmitter/receiver pairs. The vertical axis gives the scattered field relative to the direct field for the transmitter/receiver pair located at the midpoints of their respective sides. The zero value, corresponding to no component of the scattered field in the receiver direction, occurs when the transmitter and receiver are located approximately at right angles with respect to the extended target.

Figure 4-9 is a three dimensional depiction of the currents at the sample locations on the target of Figure 4-6. The active transmitter is located on the left side of the imaging square shown in Figure 4-5 horizontally across from the target. The current magnitude and direction are shown as line segments directed away from the corresponding sample point in the figure. It should be noticed that each current lies in the local plane of the surface at the sample point.

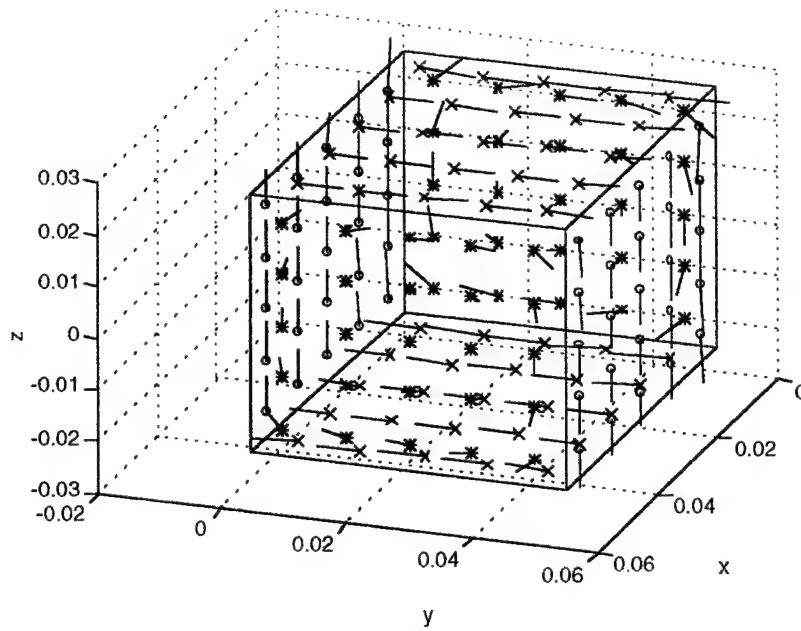


Figure 4-9: Target currents at the sample points on the target

Figure 4-10 illustrates a projection of Figure 4-9 in a vertical plane perpendicular to the imaging square of Figure 4-5. The transmitter is located on the left side of the square in a horizontal line with the center of the target. The incident field in this projection is therefore pointed toward the viewer. Notice that the currents on the face shown curl so as to produce a field that opposes the incident field.

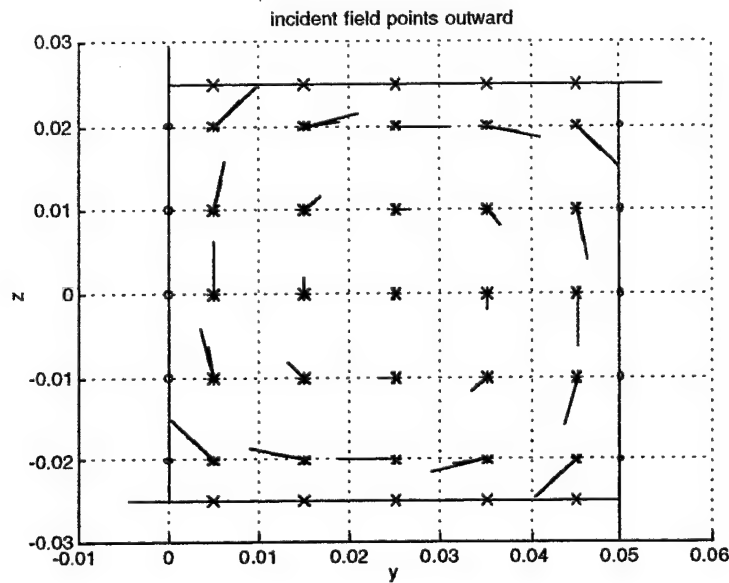


Figure 4-10: Projection of Figure 4-9 in a vertical plane perpendicular to the square in Figure 4-5.

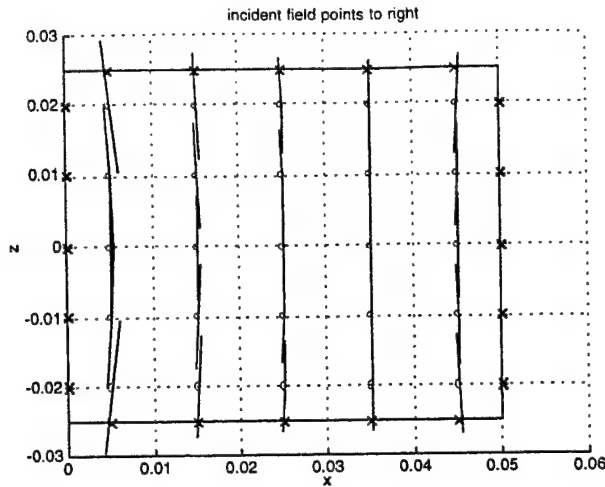


Figure 4-11: A projection of Figure 4-9 in a plane parallel to the imaging square

Figure 4-11 illustrates a projection of Figure 4-9 in a plane parallel to the imaging square. Line segments for the currents on the trailing face, which are the negatives of those on the leading face, show through in this projection making the line segments appear centered on the sample points. The transmitter is located 0.5 m to the left of the object. The incident field points to the right. Notice the diminution in the current and the changing tilt of the currents looking left to right.

A more complex example of a metallic target was designed in the shape of a pistol as shown in Figure 4-12. The figure shows the target subdivided into separated triangular patches. In the actual model, the patches are contiguous. The length of the barrel (x direction) is 20 cm, its width (y direction) is 5 cm, and its thickness (z direction) is 2 cm. The distance from the bottom of the handle to the top of the barrel is approximately 15 cm. The handle makes an angle of 105 degrees with respect to the barrel. The method of moments was used to model the scattering by this target for the system geometry described in Figure 4-5.

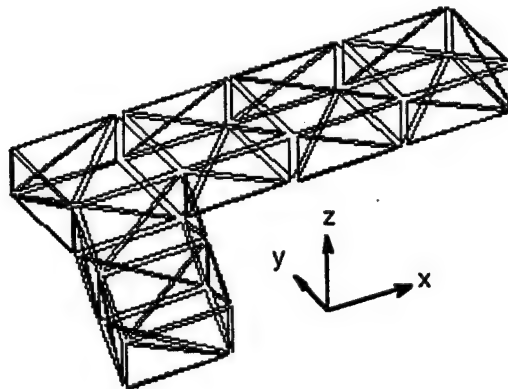


Figure 4-12: A complex geometry target modeled with Method of Moments

In determining the scattering data, the target was oriented horizontally with the inside corner between the handle and the barrel located approximately at the center of the frame. One side of the target was contiguous with the plane of the frame.

The singular value decomposition imaging algorithms were applied to the scattering data calculated with the method of moments. The resulting image is shown in Figure 4-13. The numbers around the periphery refer to locations of the transmitter/receivers.

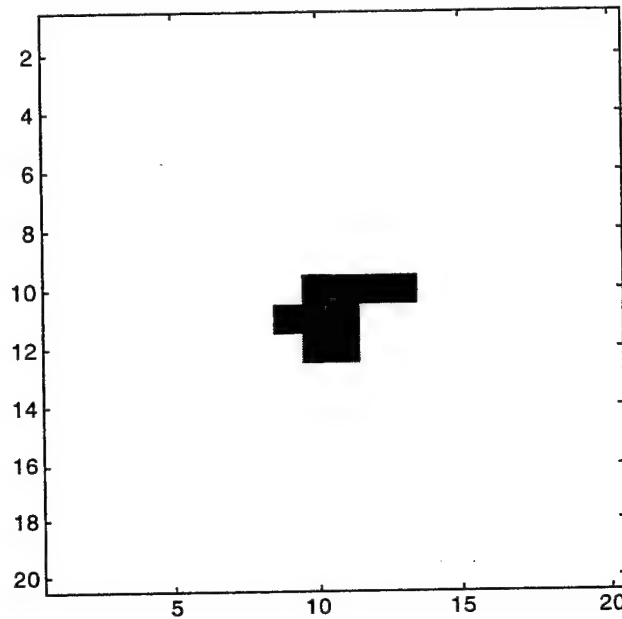


Figure 4-13: Image of pistol in Figure 4-12 computed from method of moments

4.3 Sensor Response

In determining the sensor response for the imaging system, we assume the sensor to be a magnetic core solenoid. (For an air core solenoid the permeability has its free space value.) Then the field in the core is given in terms of the component of the free space field parallel to the solenoid:

$$B_{\text{core}} = \frac{\mu}{\mu_0} B_1 \quad (4.23)$$

For N windings on the solenoid, the current it produces is given by:

$$I = \frac{1}{R} N A B_{\text{core}} \omega \quad (4.24)$$

where R is the solenoid resistance, A is its area, B_{core} is the field given by Equation 4.23, and ω is the angular frequency of the field.

4.4 Simulation Summary

We have developed numerical models capable of accurately simulating the sensor responses to magnetic fields produced by metallic or ferrite types of targets in the presence of a magnetic source field and have also developed an analysis for lossy dielectric targets that will be modeled in the next phase of the research. The target geometry is arbitrary as are the locations of the transmitter and receiver. The results of our magnetic field simulations have been used to assist in the determination of an optimum image reconstruction algorithm, as well as for investigation of different portal geometries.

5.0 Image Reconstruction

Commonly employed image reconstruction techniques rely on the concept of a projection. As illustrated in Figure 5-1 a projection is formed by combining a set of line integrals with each line integral representing the measurement of a physical value along a path joining a given transmitter and detector.

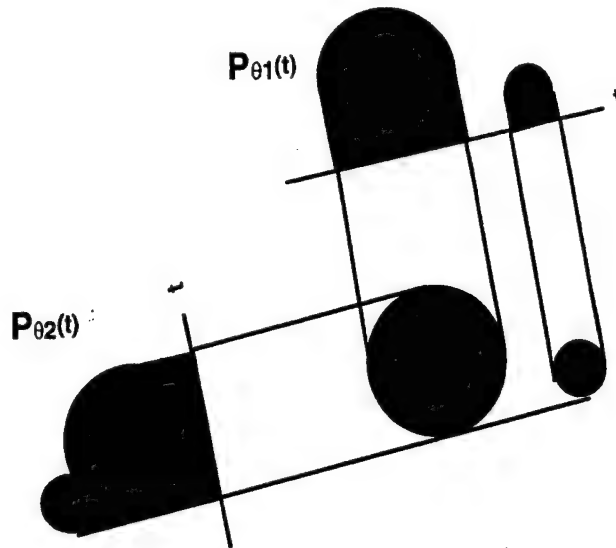


Figure 5-1 Illustration of the concept of a projection. In this example each projection $P_{\theta}(t)$ is formed by combining a collection of parallel line integrals.

Typical examples of this type of data are the attenuation of a gamma ray or acoustic beam. In each case it is generally assumed that the effect of portions of the object which do not lie along a line connecting a given transmitter and detector do not contribute significantly to the line integral. Where these conditions hold Fourier transform techniques may be applied in a very efficient manner to yield high quality images.

The LFMI method differs significantly from other more traditional tomographic techniques in that a given transmitter detector pair sample all regions of the object. As a result, much of the methodology which has been developed to deal with image reconstruction involving projections is not applicable and algebraic techniques are required. Algebraic techniques involve dividing the region of interest into discrete regions (pixels) and defining a set of algebraic equations which relate the unknowns(pixels) to physical

measurements. The resulting matrix equation may be solved by either iterative techniques or by use of conventional matrix theory.

In practice, the size of the resulting matrix as well as the nature of the data limit the method of solution. For instance, it is not unusual to find that for a given set of measurements (even for the case where the system is overdetermined) the matrix is very often singular or at least ill-conditioned. Because of this, standard matrix inversion techniques often fail. Similarly, applications involving very large matrices can be very unwieldy in standard computer systems and problems involving roundoff error during matrix manipulations can become significant. Two methods exist to handle these types of matrix systems. For very large matrices iterative techniques have been developed. While these techniques provide a solution the solution is not guaranteed to be a minimum in the least squares sense. For reasonably sized matrices (reasonable on the scale of the memory management capacity of a desktop microcomputer a method known as Singular Value Decomposition (SVD) exists. Several variants leading to increased resolution and the ability to handle larger systems have been developed.

5.1 General Iterative Solution

For the general matrix equation

$$A_{m \times n} \cdot x_{1 \times n} = b_{1 \times n} \quad (5.1)$$

a solution may be thought of as a point in n-dimensional space. In this space each equation represents a single hyperplane and the intersection of all the hyperplanes represents the solution. Iteratively the solution may be found by first assuming a best value then projecting this value onto the first hyperplane. This value is then reprojected onto the next hyperplane and so on. If a unique solution exists this technique will converge to that point. This method is illustrated graphically for a two dimensional case in the Figure 5-2 below.

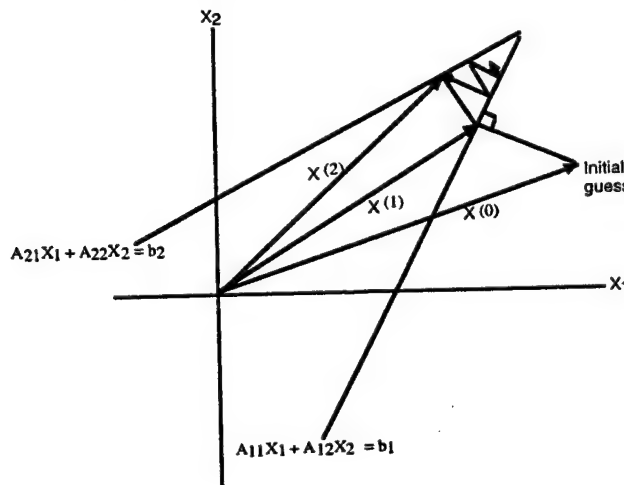


Figure 5-2 Iterative procedure for solution of a two dimensional matrix equation. An initial guess $X^{(0)}$ is assumed. This solution is then projected onto the first hyperplane and a new solution $X^{(1)}$ is obtained. This procedure is repeated until the solution converges to a single value.

For computer implementation the iterative method can be written as

$$\Delta x_j^{(i)} = x_j^{(i)} - x_j^{(i-1)} = (p_i - q_i) \cdot A_{ij} / \sum_{k=1}^N A_{ik}^2 \quad (5.2)$$

where p_i is the measured data for the i th equation and q_i is the computed data from the $(i-1)$ th solution. The correction to the j th pixel is obtained from the difference between the actual and the computed data with suitable normalization applied. This method is quite general but it is easily seen that for noisy data (no unique solution) the method will not converge to a single point and some care must be taken to terminate the iterative procedure correctly. This solution does not guarantee a solution to be a minimum in the least squares sense.

5.2 Singular Value Decomposition

The singular value decomposition (SVD) algorithm is based on a fundamental theorem of linear algebra which states that for the general matrix equation

$$A \cdot x = b \quad (5.3)$$

A can be decomposed into a product of three matrices

$$U_{m \times m} \cdot W_{n \times m} \cdot V_{n \times n}^T \quad (5.4)$$

where U and V are column orthogonal,

$$U^T \cdot U = V^T \cdot V = 1 \quad (5.5)$$

and W is a diagonal matrix. Clearly

$$A^{-1} = V \cdot \{diag(1/W)\} \cdot U^T \quad (5.6)$$

and

$$x = V \cdot \{diag(1/W)\} \cdot U^T \cdot b \quad (5.7)$$

This decomposition can be accomplished even if the matrix A is singular. Physically the columns of matrix U whose same numbered elements W_j are nonzero correspond to an orthonormal set of basis vectors that span the range of A . Similarly the columns of V whose same numbered elements W_j are zero form an orthonormal set of basis vectors for the nullspace.

The ability of a matrix to produce stable solutions to a system of equations may be expressed in terms of its condition number, defined as the ratio of the largest element of W to the smallest element. Smaller condition numbers indicate more stable solutions. We have found that LFMI matrix condition number is a function of the number of pixels included in the imaging region as well as the distances between them. It is also a function of the number, location and orientation of transmit/receiver pairs used in the measurements.

A great advantage of the SVD method is that even for a singular matrix a solution may be found. This solution is guaranteed to be minimum in the least squares sense.

As discussed previously for LFMI applications the matrix A is determined strictly by geometrical considerations and a predetermined sequence of sensor measurements. The inversion can therefore be performed prior to runtime and the generalized inverse stored.

The SVD method provides a number of advantages. In particular it :

- is well behaved
- easily implemented
- applicable in both underdetermined and overdetermined applications
- yields a solution which is a minimum in a least squares sense
- can be performed prior to runtime

Two generalized reconstruction methods employing the SVD method have been developed for LFMI applications.

5.3 SVD Multi-Step Method

Numerical simulations of the LMFI system have revealed that a single step algebraic reconstruction algorithm produces poor reconstructions for data with low signal to noise ratio (SNR). A multi-step version of this algorithm has been formulated which provides good reconstructions for noise levels up to ~ 5% of signal.

The multi-step version of the reconstruction algorithm consists of:

- Applying the stored reconstruction matrix to obtain a first approximation of the image
- Reduce column rank of the original matrix by including only those columns corresponding to pixels above a given value.
- Calculate a new matrix from a reduced set of equations (via SVD method) and apply to data

Typically the process converges after only a few applications. The first image reconstruction step can be quite fast as the resulting matrices can be pre-calculated and stored. For reasonably sparse images the subsequent SVD calculations are quite fast. The true power of this multi-step procedure is that each of the resulting projection matrices is increasingly overdetermined. An example of this method applied to real data is shown in Figure 5-3 below.

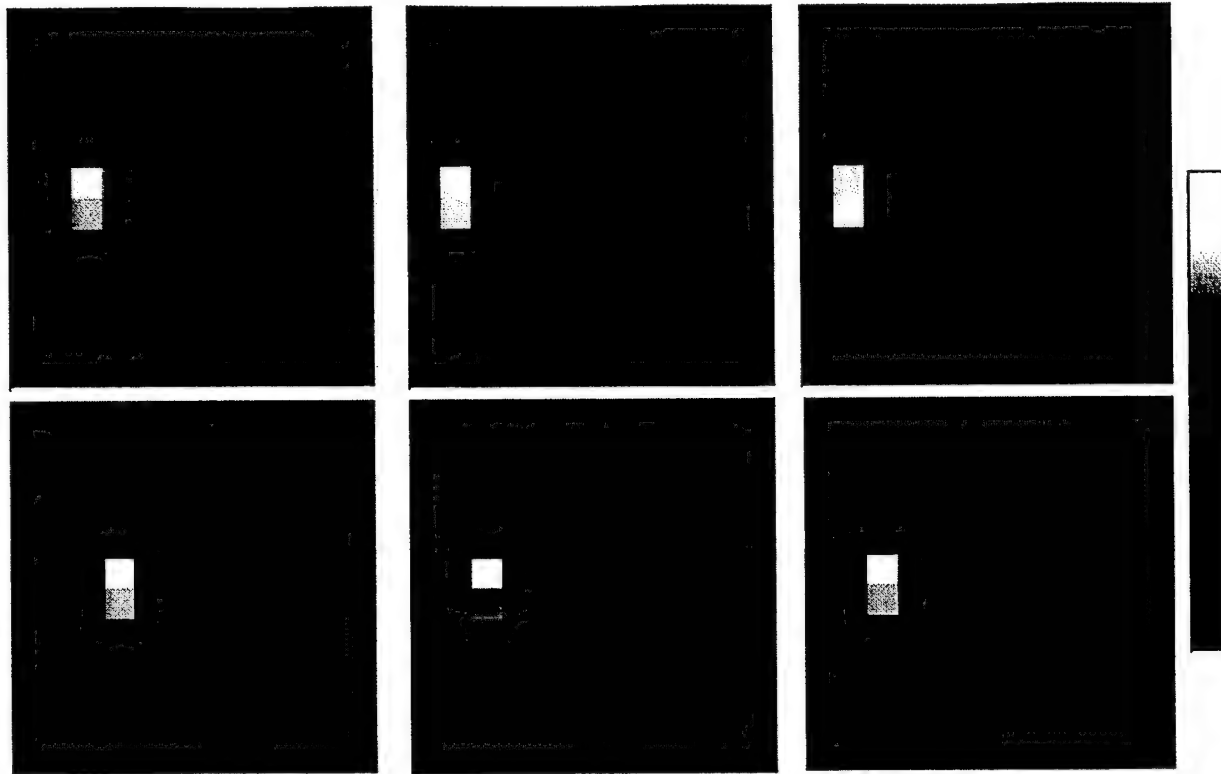


Figure 5-3 Illustration of the multi-step image reconstruction process. The object is a 4" cube of aluminum. Note that the last two images are almost identical, indicating that the reconstruction algorithm has converged on the final image.

5.4 Hierarchical Image Reconstruction

Where large matrices are involved and where computational time is critical a hierarchical approach to image reconstruction has been developed. In this approach the entire interior region is initially imaged at a low resolution. Non-contributing regions of the image (pixels) are then removed from the matrix and the remaining area is then reimaged at higher resolution. This process is repeated until the desired resolution is achieved.

A schematic of the hierarchical imaging approach is illustrated in Figure 5-4. The example portal in the figure, which we use for numerical modeling, is one meter on each side, with 20 transmit/receive dipoles located on each side with a 5 cm spacing. The initial matrix reconstructs a 5x5 pixel array with 20 cm resolution (linear dimension of pixel). After reconstruction, some pixels are normally found to be non-contributing and are removed from the system of equations. The remaining 3x3 region, shown in gray, can then either be reimaged at the same 20 cm resolution, and additional non-contributing pixels removed, or the pixel size can be directly reduced to 10 cm to produce a 6x6 matrix. After again eliminating non-contributing pixels the light gray area is imaged at 10 cm and then 5 cm resolution. Iterating this procedure once more yields a 5x5 pixel region imaged with a 2.5 cm (1") resolution. This approach has the advantage that convergence is generally more rapid and, because of the initial low resolution, may handle larger systems than the iterative reconstruction method.

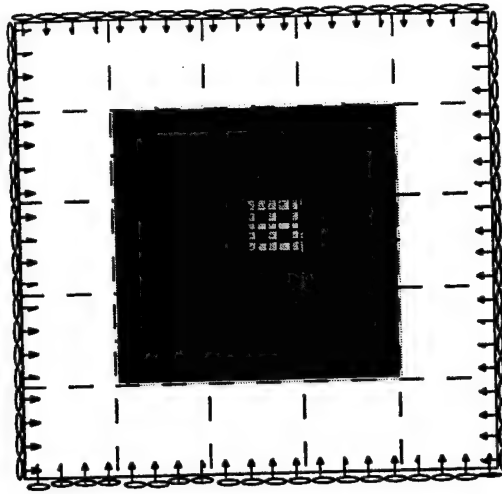


Figure 5-4 Example of hierarchical imaging approach, showing successive areas in the portal being imaged at increasingly finer resolution. The final image is the rectangular array of four one-inch squares slightly offset from center.

5.5 Spatial Resolution Simulation

For simulation, the 1 m^2 portal and transmit/receive arrangement shown in Figure 5-4 was used. In the simulations that were performed, two methods were employed in creating the transmit/receive pair simulated measurements used for the \mathbf{S} -vector in the right-hand-side of Equation 3.10. The point-dipole method assumes that independent, non-interacting dipoles are present in the plane of the portal at the locations of the objects and uses the known matrix \mathbf{G} to calculate the right-hand-side \mathbf{S} -vector of transmit-receive pairs. The method of moments (MOM) treats the targets as conductive objects and calculates the currents on the object surfaces for each transmitter location. The currents satisfy the perfectly-conducting boundary conditions on the object's surfaces and include all interactions between the object and the transmitter field, as well as the mutual interactions of neighboring objects. The fields produced by these currents at each receiver are then computed to ascertain the \mathbf{S} -vector.

Four separate simulation cases were investigated. We first considered noiseless point-dipole reconstruction as an ideal case. We performed the next series of calculations using the method of moments, again without including random noise. In both of these cases, the reconstructed image of the 2×2 array of cubes was very good. Because the differences between the point-dipole and MOM results were slight, and because the MOM is computationally more complex, we opted to investigate the sensitivity to noise on the signal with just the point-dipole approach. Finally, we added additional transmitters and receivers in different spatial orientations to ascertain the effect of full vector magnetic field measurements. The choices of transmit/receive pairs used in the different simulations included a set of 182 pairs of inward-pointing orientation used for the first three cases and a larger set that included all 3 orientations for the last case. We learned in the process of using the different sets that we can improve our imaging results by varying the set of transmit/receive pairs in the reconstruction and that the inclusion of other receiver orientations can be beneficial. Due to time constraints, we were not able to find an optimum set of transmit/receive pairs; the results were obtained using a good, but nonetheless sub-optimal set.

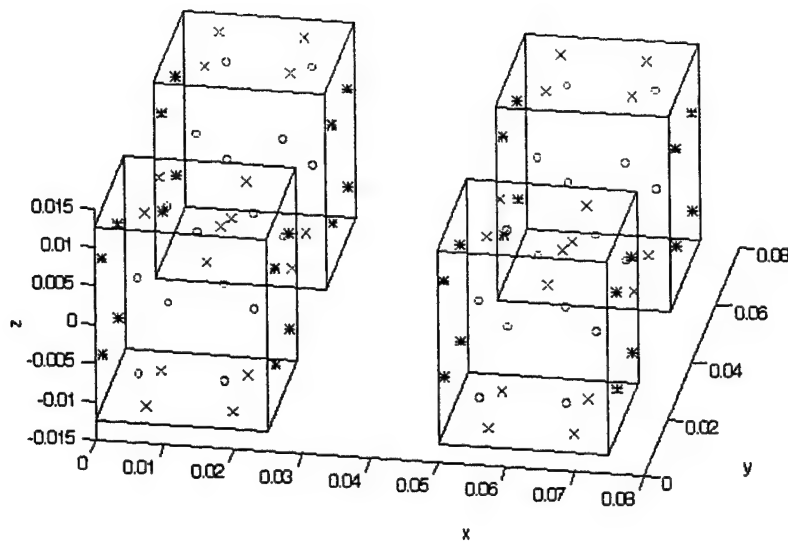


Figure 5-5 Three-dimensional diagram of the 2x2 array of cubes used as a model object in the LFMI reconstruction simulations. The cubes are 1" on a side and are placed on 2" center-to-center spacings.

Figure 5-5 depicts the object design used in the MOM computation of the simulation. The design consists of 4 identical conductive 2.5 cm cubes with centers spaced 5 cm apart. The cubes lie in the first quadrant, straddling the $z=0$ plane. Red sample points for the MOM current calculations are on the top and bottom surfaces, green points on the front and rear surfaces, and blue points on the left and right surfaces. For the point-dipole approximation the object is the projection of the cubes in the $z=0$ plane.

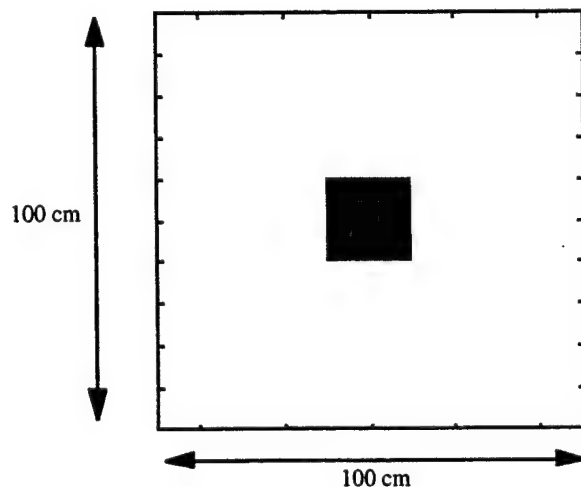


Figure 5-6 Entire portal interior imaged with a 5x5 array of 20 cm pixels

Figure 5-6 shows the image produced by the target using the point-dipole method at 20 cm resolution with the entire portal covered by a 5x5 grid of pixels. The outermost pixels in the image are deemed non-contributory and could be eliminated from the reconstruction matrix.

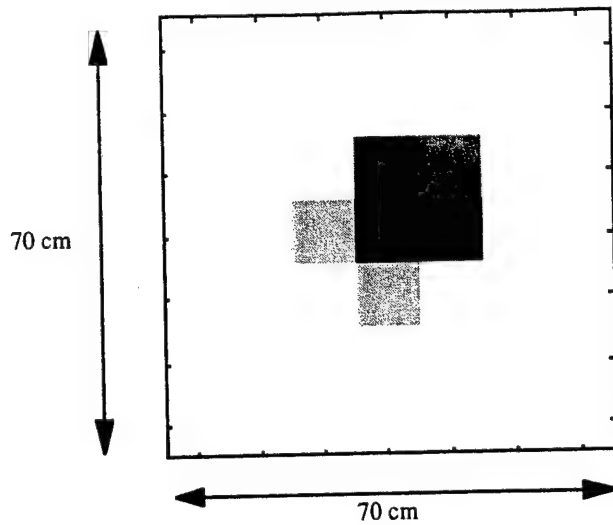


Figure 5-7 Central 70x70 cm area of portal imaged with a 7x7 array of 10 cm pixels.

Figure 5-7 depicts the dipole method image produced for a centrally located 7x7 grid of 10 cm pixels. The two outermost rings of pixels were eliminated based on this image.

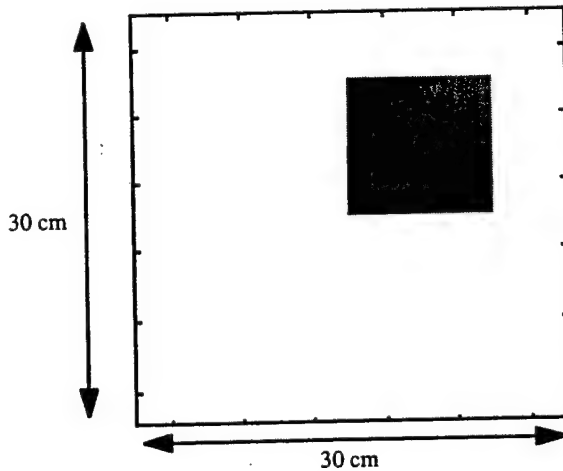


Figure 5-8 Central 30x30 cm portion of portal imaged with a 6x6 array of 5 cm pixels.

Figure 5-8 illustrates the image that results at 5 cm resolution after reducing the imaging area to a central 30 cm square and using a 6x6 pixel array. Imaging the part of Figure 5-8 with the highest response at higher resolution (2.5 cm) yields an accurate image of the original object, as depicted in Figure 5-9.

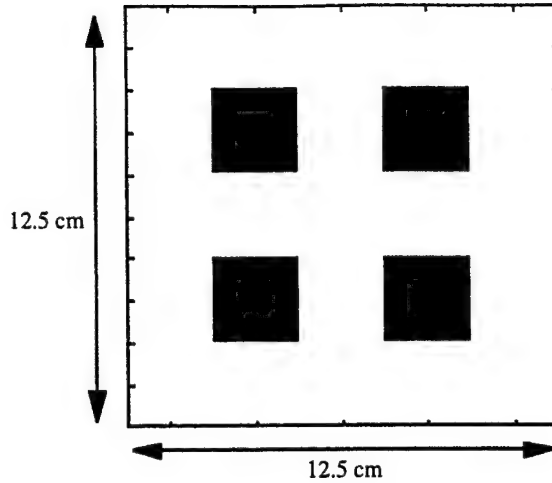


Figure 5-9 Image of a 12.5 cm x 12.5 cm portion of the portal, which includes the darkest pixels in Figure 5-8, imaged with a 5x5 array of 2.5 cm pixels.

Although the results shown in Figure 5-9 are impressive, and clearly demonstrate 1" image resolution, they were obtained by a simulation method with some inherent assumptions, namely the absence of any dipole-dipole interaction between neighboring parts of the object. While we believe that this assumption is a good one, we have the ability to model the interaction comprehensively by using the method of moments. The MOM method was used to produce the image shown in Figure 5-10 for the central 7.5 cm x 7.5 cm region of the portal and 2.5 cm spatial resolution. The similarity of these two reconstructed images shows that the assumption of small dipole-dipole interactions is a good one.

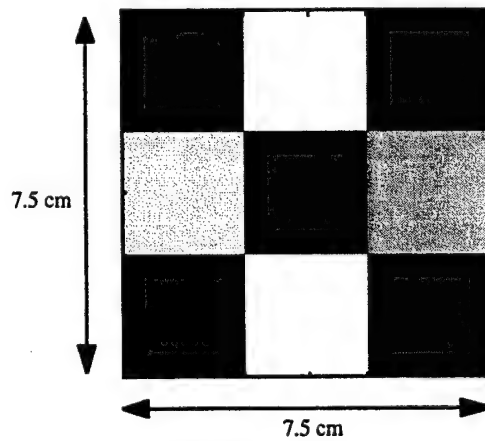


Figure 5-10 Same image as reconstructed in Figure 5-9, but using the method of moments to generate the received field strengths.

Finally, we examine LFMI images produced with the point-dipole method when a varying amount of Gaussian noise is added to the values for the transmit/receiver pairs. This noise simulates the effect of finite signal-to-noise ratio in a real measurement. The noise was calculated as a fraction of the rms value of the right-hand-side **S**-vector

multiplied by a normally distributed random variable with unit variance. The noise for each simulated receiver is independent of others.

Figures 5-11, 5-12, and 5-13 show images of the object with added noise of 1%, 0.5%, and 0.1%, respectively. The two images for each figure are different realizations of the random noise, generated by a change of the random number generator's seed value. Note that with 1% added noise, there is some probability that the object will not be imaged with sufficient fidelity to determine its shape. Lower noise levels allow good representations of the object to be obtained.

Figure 5-14 shows that a degree of image improvement can be obtained by measuring all the components of the magnetic field with additional receivers in mutually-orthogonal orientations. Full vector field measurements allow a tradeoff between operation at lower signal-to-noise ratios and the added computational burden of additional receiver measurements.

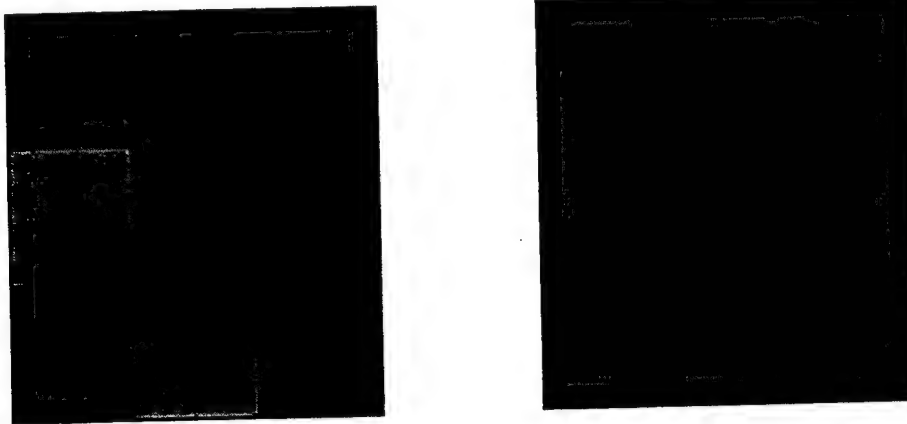


Figure 5-11 Image reconstruction of the 4-cube object with the point-dipole method, and 1% gaussian noise added to the simulated receiver measurements. The left and right images are two separate realizations of the random numbers used to generate the noise. The imaged area is 7.5 cm x 7.5 cm in size and contains a 3x3 array of 2.5 cm pixels.

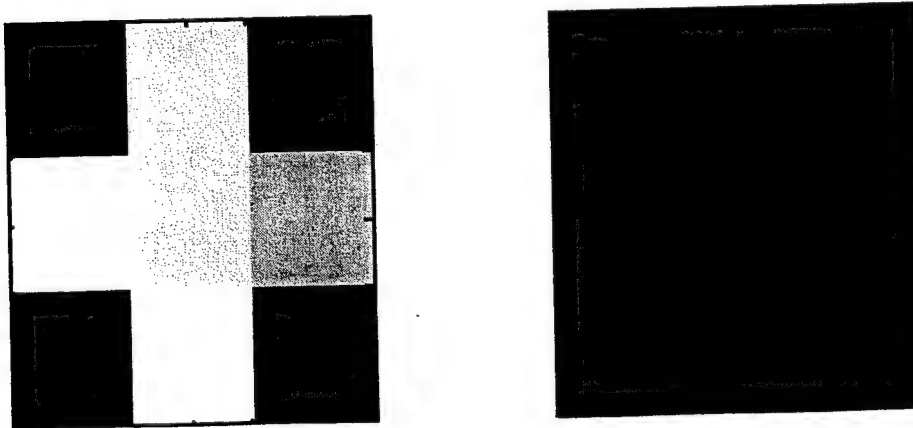


Figure 5-12 Same as Figure 11, except 0.5% additive gaussian noise.

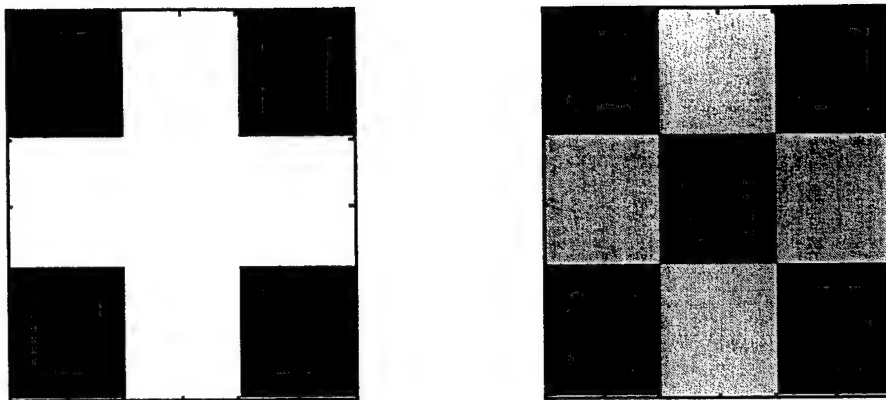


Figure 5-13 Same as Figure 11, except 0.1% additive gaussian noise

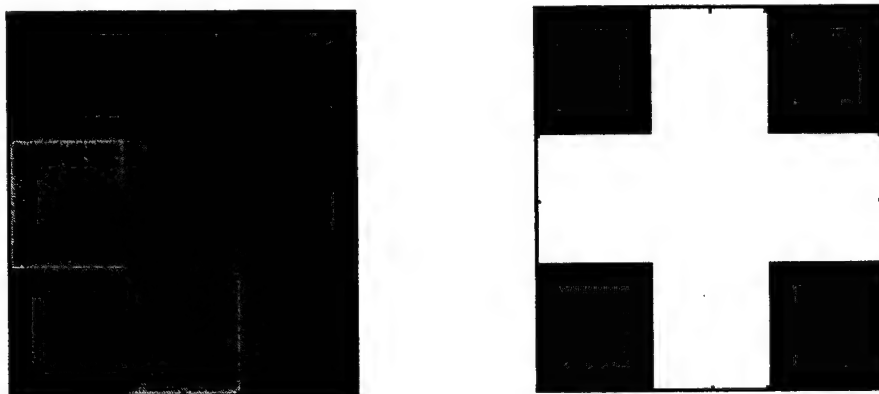


Figure 5-14 Image reconstruction of the 4-cube object using the point-dipole method with 3 orthogonal orientations of receiver coils, and 0.5% gaussian noise added to the simulated receiver measurements. The left and right images are two separate realizations of the random numbers used to generate the noise. The imaged area is 7.5 cm x 7.5 cm in size and contains a 3x3 array of 2.5 cm pixels.

5.6 Discussion of Results

The LFMI simulation results clearly show that a spatial resolution of one inch is achievable, even when a moderate amount of random noise is present on the receiver measurements. The previously-planned improvements to the receiver circuitry, along with local signal processing at each receiver, are projected to result in a signal-to-noise ratio similar to that modeled in the simulation results, with a processing time that allows real-time imaging in the portal. Further, the hierarchical image reconstruction method should simultaneously reduce the required computational load per image, and increase the final fidelity of the image. This is because at every refinement step, all measurements are being used to determine an increasingly smaller set of unknowns; the system of equations becomes more determined at each step. This technique tends to reduce the effect of noise, as the final image is the “best fit” to the measurements in the least-squares sense.

A side-effect of the recent spatial resolution simulation runs is the extension of the current modeling framework to include receiver coils with orientations other than normal to the portal walls. This full magnetic vector modeling ability is now able to assist in our investigation of the out-of-plane response to objects. We anticipate learning how we might use the out-of-plane information to determine object passage rates through the portal, as well as transport direction.

6.0 Experimental Results

In order to evaluate the efficacy of the low frequency magnetic imaging technique a breadboard test apparatus was constructed. Field measurements, materials response, electronics sensitivity and image resolution were evaluated.

6.1 Breadboard LFMI Apparatus

A cartoon of the breadboard system appears in Figure 6-1. The portal is a wooden frame measuring 5 ft. wide by 7 ft. tall. 12 magnetic-dipole antennas with their associated transceiver circuitry are mounted on one side of the portal. The transceiver circuit boards were only partially populated with components because they were used solely as receivers during our testing. The receivers were controlled via a daisy-chained digital bus from the computer. The magnetic field amplitude seen by a particular receiver is obtained by commanding the receiver circuitry to connect the antenna to the on-card low-noise amplifier, and then commanding the card to output the signal on a multi-drop analog bus. The analog signal is connected to a commercial lock-in amplifier which extracts the signal in phase with and at the transmitter frequency. The "external" lock-in amplifier was used instead of on-board phase-sensitive detection, which will appear in the prototype LFMI sensor.

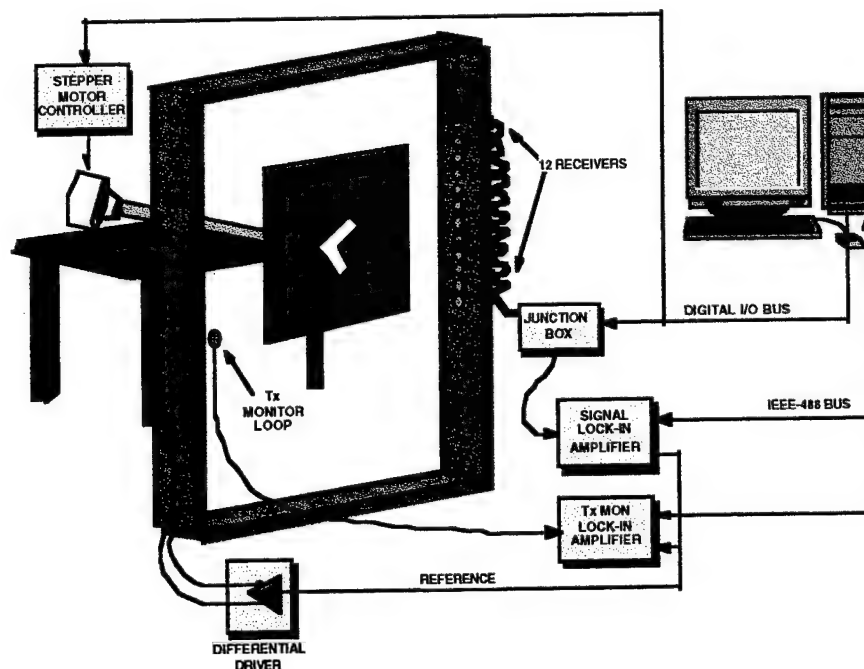


Figure 6-1 The experiment is controlled by a 133 MHz IBM-compatible computer running the Windows NT operating system. A custom 32-bit C++ application orchestrates data collection, motor actuation, and image reconstruction. Data are acquired from the lock-in amplifiers (or any other adjunct instrument) via an IEEE-488 interface for maximum flexibility.

Directly across from the array of 12 receivers is mounted another transceiver card configured as a transmitter. The timing signals for the transmitter, which determine its frequency and phase, originate from the reference output of the master lock-in amplifier. A separate, shielded, single-loop H-field antenna is mounted adjacent to the transmitter antenna as an independent monitor of transmitted magnetic field strength during tests. This antenna is fed to another lock-in amplifier, whose reference is phase-locked to the master lock-in.

The objects to be imaged by the LFMI sensor are placed on a turntable in the center of the portal which is turned in well-defined angular increments by a computer-controlled stepping motor. To minimize the number of transceiver circuit cards in the breadboard apparatus, a fixed transmitter-receiver geometry with a rotating object was chosen. This is analogous to the fully-populated sensor with a fixed object, where measurements are taken over a range of different angles by programming different transmitter-receiver pairs to make measurements.

The experiment is controlled by a 133 MHz IBM-compatible computer running the Windows NT operating system. A custom 32-bit C++ application orchestrates data collection, motor actuation, and image reconstruction. Data are acquired from the lock-in amplifiers (or any other adjunct instrument) via an IEEE-488 interface for maximum flexibility.

6.2 LFMI Magnetic Field Measurements

The LFMI reconstruction algorithm assumes that the transmitter magnetic field pattern is that due to an ideal magnetic dipole. Any deviations from this pattern will be reflected in errors in the reconstructed image. To test the transmitter field pattern a receiver coil, oriented alternately with its axis parallel and anti-parallel to the transmitter coil, was placed at a fixed distance normal to the transmitter coil. Measurements of the local magnetic field were made as the receiver coil was translated normal to the transmitter coil. The orientations were as shown in Figure 6-2. The measurements were performed with the receiver both relatively close to the transmitter coil and relatively far from the transmitter. As shown in Figure 6-2 all measurements were found to be essentially those of an ideal magnetic dipole.

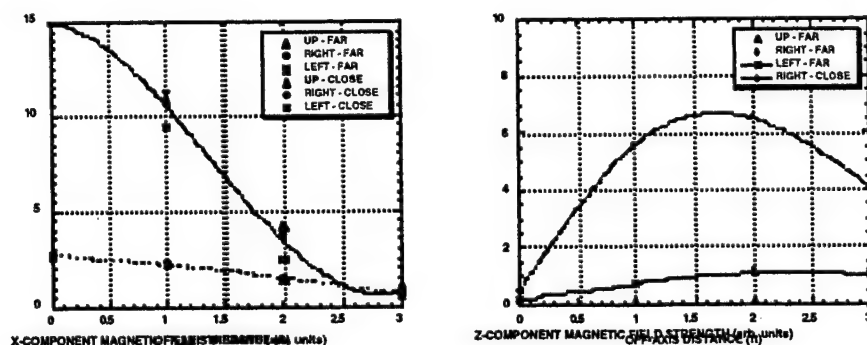


Figure 6-2 Magnetic field measurements made both on-axis and off-axis with respect to the transmitter. The transmitted field is characteristic of a pure dipole emitter.

6.3 Material Response Measurements

The response of the LFMI sensor to different types of materials was investigated by inserting 2" cubes of the materials into the center of the portal, and measuring the change in the receiver signal that was coaxial with the transmitter. The results of these measurements appear in Figure 6-3. Basically, all conductors caused a large change in the detected signal. Graphite, which is not included in Figure 6-3, showed a response equivalent to aluminum. The stainless steel data is somewhat lower than the other metals because its ferromagnetic properties, even at the relatively high excitation frequency (90 kHz) cause a response opposite in sign to those due to induced eddy currents on the cube's surface. These two effects partially cancel each other, resulting in a lower response.

Of significance is the small response to a saturated NaCl solution in water. Based on this measurement, human tissue, which is less conductive than a saturated salt solution, is expected to cause an insignificant response. Indeed, people walking through the portal carrying no conductive objects are not detectable. This indicates that weapons concealed in body cavities are visible to the LFMI detector, and can be imaged.

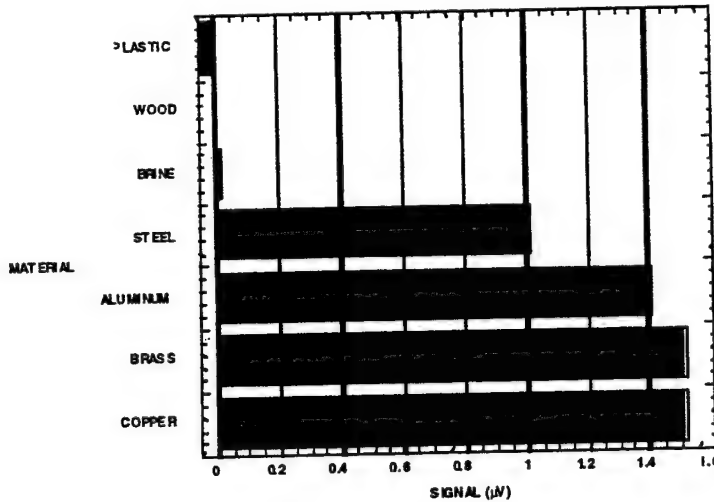


Figure 6-3 LFMI receiver response to different materials

6.4 Preliminary Imaging Measurements

To test the hierarchical and iterative image reconstruction methods, a hollow cube of aluminum 4" on a side was placed at various locations on the turntable in the plane of the LFMI portal. Imaging of the cube was accomplished by first measuring the response of each receiver with no object present. With the object in place, the local magnetic field at each of the 12 receivers was then measured, the turntable rotated, and the measurement repeated. This process continued for a total of 12 different angular positions over a total angular range of 180 degrees. The image was reconstructed assuming a 2" x 2" pixel area. The results, clearly demonstrating four inch resolution, are shown in Figure 6-4 below.

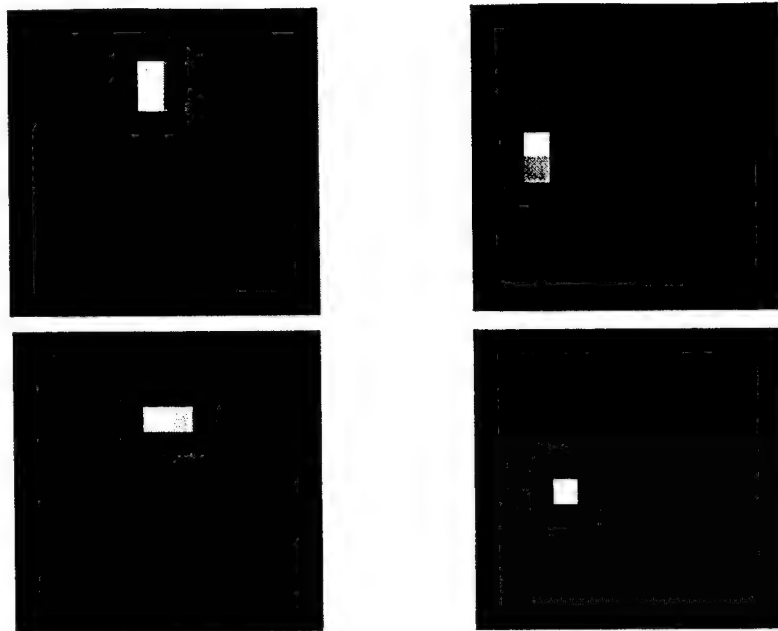


Figure 6-4 Images of the 4" aluminum cube placed and imaged at four different locations in the portal

Similar measurements performed on aluminum cans (2.5" X 4.75") were also performed and demonstrate that the current system is capable of 2" resolution. The results are shown in Figure 6-5.

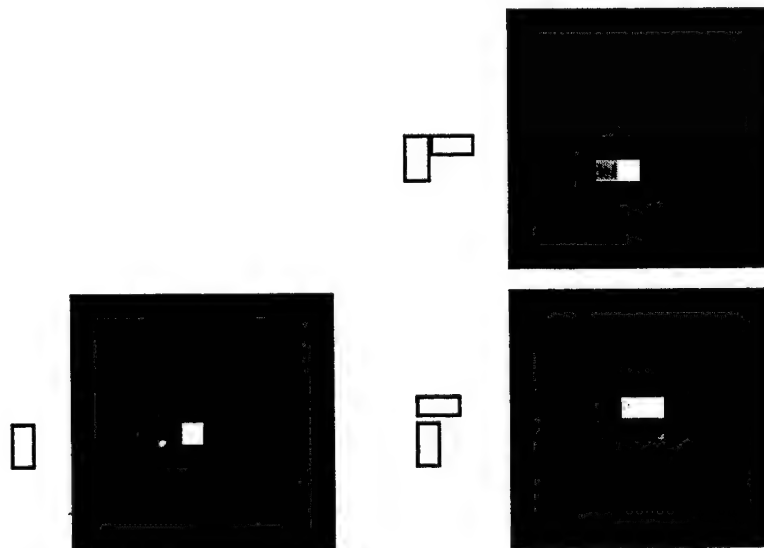


Figure 6-5 Images of aluminum cans (empty) placed in various orientations within the sensor portal. The imagery clearly show 2" spatial resolution.

As a test of the LFMI system's ability to image more complex objects, measurements were made of an aluminum model of a large gun-shaped weapon. The

weapon had a barrel and handle with a 2" square cross section 10" and 5" long, respectively. The resulting reconstructed image appears in Figure 6-6. The reconstruction has an additional imaging artifact atop the barrel. This artifact is believed to be the result of receiver noise, use a sub-optimal set of transmitter-receiver measurements and a limited number (12) of distinct angular orientations of the object turntable.

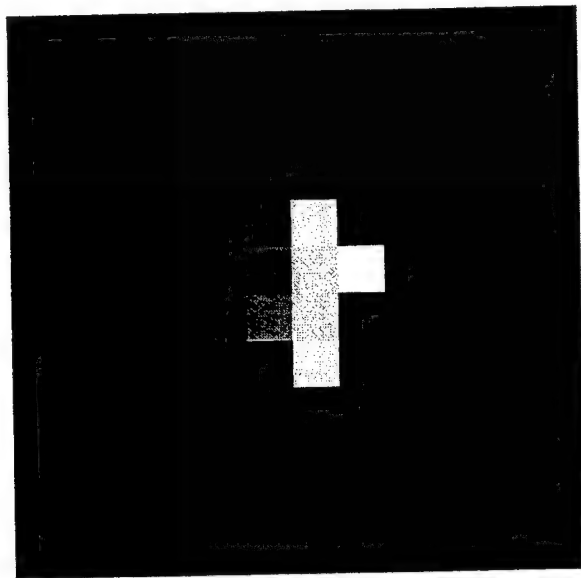


Figure 6-6 Reconstructed image of aluminum gun

Achievable image resolution is a complicated combination of measurement signal-to-noise ratio, signal processing, measurement geometry, and image inversion method. During these tests it was determined that the major limiting factors in the resulting image resolution were the stability and noise present in the LFMI receiver signal. Because the test system was designed for maximum flexibility as opposed to speed of data acquisition baseline shifts in the receiver signal were a source of significant errors. Similarly it was observed that occasional very large excursions in receiver signal occurred for no apparent reason. When this occurred during a test, image reconstruction would consistently fail. These baseline shifts in the receiver signal, both large and small, were found to increase during the daylight hours and to significantly decrease or disappear in the early morning hours. The source and nature of this noise is discussed in the next section.

6.5 Electronic Sensitivity

There are two components to the noise observed in the output of the LFMI receiver. The first is gaussian-distributed, white-spectrum fluctuations in the voltage output. This component has a measured power spectral density of about $10^{-14} \text{ V}^2/\text{Hz}$, and is consistent with the observation of approximately 100 nVrms fluctuations within our 1 Hz bandwidth. This noise is primarily due to the input stage of the operational amplifier used in the receiver, and is not large enough to preclude the imaging of metal in the portal.

The second noise component is typified by an abrupt change in receiver output level. The change in level occurs on time scales less than one second, affects all receivers simultaneously, and is generally in the range of 0.5-20 μV . The step-noise tends to occur randomly throughout the day, but usually lessens or disappears completely during the early morning hours between midnight and dawn. This noise component, because its magnitude is comparable to the signal, is disruptive to the imaging process.

A number of measurements have been made to determine the source of the noise. Figure 6-7 shows the signal output from all twelve LFMI receivers as a function of time over a 15 hour interval. During this time the LFMI transmitter was turned off. The data display the 100 nVrms fluctuations from the receiver amplifier, but do not exhibit the step noise. It was determined that the LFMI transmitter must be on before the step noise appears. These data show that external radio-frequency or magnetic dipole interference, such as from radio stations, etc. are excluded from the measurement. This is mainly due to the signal processing, which rejects all signals except those in a 1 Hz band (centered at 90 kHz) that are phase-locked to the reference waveform.

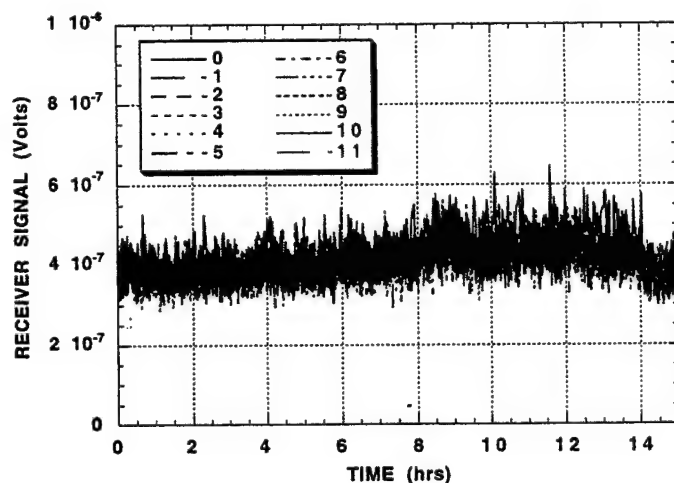


Figure 6-7 Receiver signal from all twelve receivers with the LFMI transmitter turned off.

Figure 6-8 shows a typical receiver output exhibiting the step noise during a 20 hour time span with the LFMI transmitter on. Although not shown in this graph, all receiver's outputs step in the same direction at the same time, and have roughly the same magnitude. Although this would logically implicate the transmitter, the graph also shows the signal from a single-turn, electrostatically-shielded coil placed directly beneath the transmitter coil. This coil is a direct monitor of the transmitted H-field, and shows no fluctuations except for a long-term small drift (probably thermal). Efforts were made to scale the H-field monitor signal so that intentional adjustments of the transmitted field show up with the same magnitude on the monitor and the receiver. These data indicate that changes in transmitter field are not responsible for the presence of the step noise.

Another possible source for the step noise is the signal processing equipment, specifically the lock-in amplifier. A Stanford Research Systems model SR830 digital lock-in amplifier was used to process the receiver outputs. This instrument is configured to detect only the receiver signal components that are present in a 1 Hz bandwidth centered at

90 kHz, and with a predetermined phase relationship to the transmitter switching waveform. It was hypothesized that phase jitter in the reference channel or a digital anomaly might be responsible for the step noise. To test this hypothesis, the lock-in amplifier output was compared with a Hewlett-Packard model 35665A low-frequency spectrum analyzer. The spectrum analyzer was configured to measure the integrated power in a ± 5 Hz band centered at 90 kHz. As seen in Figure 6-9, both instruments observe the step noise, indicating that the signal processing is not in error.

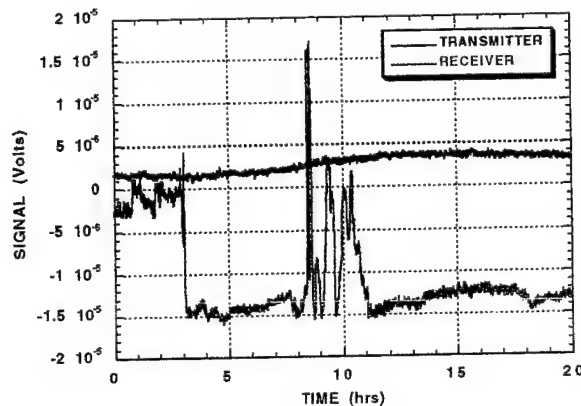


Figure 6-8 Transmitter and receiver signals over a 20 hour time period. These data indicate that changes in transmitter field are not responsible for the presence of the step noise.

In addition to the measurements plotted here, we made numerous changes to the power distribution, grounding, and signal routing of the LFMI electronics. Single-point grounding, isolation from building ground, and electrostatic shielding on all cables were installed with no reduction in the step noise.

Investigations of possible saturation of either the receiver input amplifier or lock-in amplifier were also undertaken to determine if some out-of-band stimulus was causing a nonlinearity in an electronic component. The signal directly out of the receiver coil was analyzed with a Hewlett-Packard model 8595A spectrum analyzer. Local AM and FM radio, VHF and UHF television stations, and mobile communications frequencies had observable signal, but none exceeded a -50 dBm level. There were also several signals observed below 100 kHz, presumably associated with navigation beacons, but none exceeded -60 dBm. There was also no observable peak at the coil's self-resonance frequency of approximately 1 MHz. Over the frequency range from 1 Hz to 1 GHz there was no signal with an amplitude sufficient to cause input nonlinearity of the receiver preamplifier. In addition, investigation of the signal entering the lock-in amplifier input revealed that by far the largest component was the signal from the magnetic field of the transmitter. Indeed, operation of the lock-in amplifier at a much less sensitive input level (to give more headroom for large out-of-band signals) did not result in any decrease in the step noise.

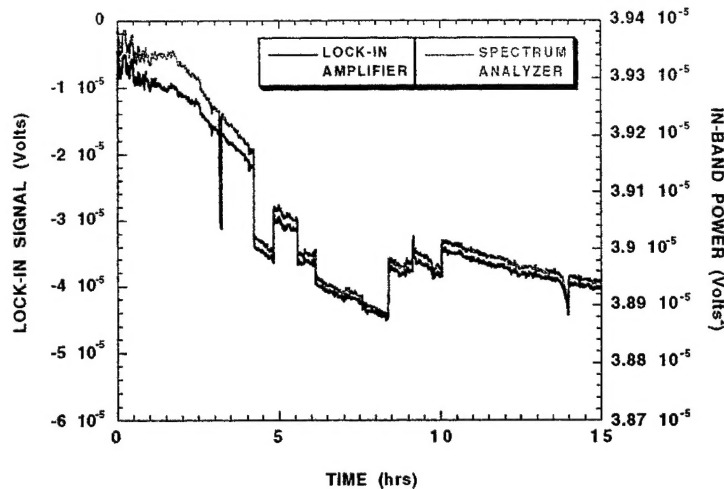


Figure 6-9 Plot of received signal from the Stanford Research digital lock-in amplifier and a Hewlett Packard low frequency spectrum analyzer.

Current plans for finding and eliminating the noise are summarized below in the form of a list of hypotheses and associated actions.

- hypothesis: electrostatic pickup of transients in LFMI transmitter
action: investigate electrostatically-shielded transmitter and receiver coils
- hypothesis: voltage fluctuation in common signal return
action: isolate both sides of receiver amplifier output, operate as true differential
- hypothesis: DC magnetic field changes affect transformer core permeability
action: test receiver without transformer, monitor DC magnetic field changes
- hypothesis: small contact resistance changes in power supply leads and contacts
action: isolate Rx, Tx rails and add more power-supply decoupling to receiver
- hypothesis: spontaneous change in transmitter radiation pattern
action: use array of single-turn loops to measure vector H-field at various locations with respect to the transmitter, construct a new transmitter antenna from rigid cable

We anticipate that the investigation of the items on this list (and any others that arise) will take approximately 3-4 weeks, and will be the first item of business upon award of the second phase of the contract. Real progress toward the phase II goals cannot commence until the step-noise issue is resolved.

7.0 Phase 2 Program Plan

Phase 2 of SPEC's development effort will result in the production of a brassboard low-frequency magnetic imaging concealed weapons detector. The detector will be capable of imaging conductive objects transported through the portal in real time, with image update rates of approximately 10 Hz. Associated hardware and software modules will provide at least a modest level of object recognition capability. A comprehensive operator interface

will display reconstructed imagery of conductive objects overlaid on standard camera video, and will allow control of most aspects of the detector operation.

The duration of the phase 2 effort is 20 months, with a schedule as shown in Figure 7-1, followed by a 2-month demonstration of the system to program sponsors, government agencies, and law-enforcement officials. Midway through the phase 2 program, SPEC plans to debut the LFMI concealed-weapons detector technology to industry at the annual American Society for Industrial Security (ASIS) show. The ASIS show is currently scheduled for September 1997, and is the focal point for new products and technology serving the security industry. It is anticipated that our synergistic relationship with Honeywell's XSM building security product will give SPEC and the LFMI technology wide exposure to commercial customers, partners, and resellers.

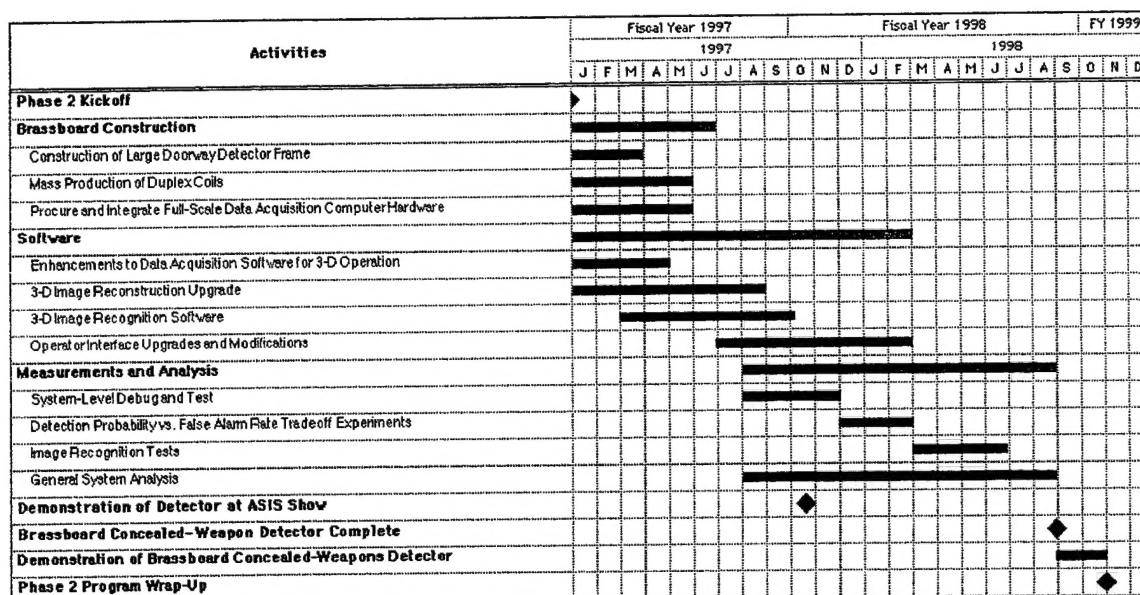


Figure 7-1 Phase 2 program schedule, showing timelines for all major proposed tasks.

DISTRIBUTION LIST

AIR FORCE RESEARCH LABORATORY/IFEA 32 BROOKS ROAD ROME, NY 13441-4114 ATTN: MR. DAVID D. FERRIS	20
SYSTEMS & PROCESSES ENGINEER CORP 401 CAMP CRAFT RD AUSTIN, TX 78746	2
AFRL/IFOIL TECHNICAL LIBRARY 26 ELECTRONIC PKY ROME NY 13441-4514	1
ATTENTION: DTIC-DCC DEFENSE TECHNICAL INFO CENTER 8725 JOHN J. KINGMAN ROAD, STE 0944 FT. BELVOIR, VA 22060-6218	2

***MISSION
OF
AFRL/INFORMATION DIRECTORATE (IF)***

The advancement and application of information systems science and technology for aerospace command and control and its transition to air, space, and ground systems to meet customer needs in the areas of Global Awareness, Dynamic Planning and Execution, and Global Information Exchange is the focus of this AFRL organization. The directorate's areas of investigation include a broad spectrum of information and fusion, communication, collaborative environment and modeling and simulation, defensive information warfare, and intelligent information systems technologies.